Renormalization functions for N_{f}=2 and N_{f}=4 twisted mass fermions

Constantia Alexandrou, Martha Constantinou, and Haralambos Panagopoulos

Phys. Rev. D **95**, 034505 — Published 27 February 2017

DOI: 10.1103/PhysRevD.95.034505

Renormalization functions for N_f=2 and N_f=4 Twisted Mass fermions

Constantia Alexandrou[a,b], Martha Constantinou[a,b,c], Haralambos Panagopoulos[a *]

a Department of Physics, University of Cyprus,
POB 20537, 1678 Nicosia, Cyprus

b Computation based Science and Technology Research Center,
The Cyprus Institute,
15 Kypranoros Str., 1645 Nicosia, Cyprus

c current address: Department of Physics, Temple University,
1925 N. 12^{th} Street, Philadelphia, PA 19122, USA

We present results on the renormalization functions of the quark field and fermion bilinears with up to one covariant derivative. For the fermion part of the action we employ the twisted mass formulation with N_f=2 and N_f=4 degenerate dynamical quarks, while in the gluon sector we use the Iwasaki improved action. The simulations for N_f=4 have been performed for pion masses in the range of 390 MeV - 760 MeV and at three values of the lattice spacing, a, corresponding to β=1.90, 1.95, 2.10. The N_f=2 action includes a clover term with $c_{\rm sw}$=1.57551 at β=2.10, and three ensembles at different values of m_π.

The evaluation of the renormalization functions is carried out in the RI$'$ scheme using a momentum source. The non-perturbartive evaluation is complemented with a perturbative computation, which is carried out at one-loop level and to all orders in the lattice spacing, a. For each renormalization function computed non-perturbatively we subtract the corresponding lattice artifacts to all orders in a, so that a large part of the cut-off effects is eliminated.

The renormalization functions are converted to the $\overline{\rm MS}$ scheme at a reference energy scale of μ=2 GeV after taking the chiral limit.

PACS numbers: 11.15.Ha, 12.38.Gc, 12.38.Aw, 12.38.-t, 14.70.Dj
Keywords: Lattice QCD, Twisted mass fermions, Renormalization functions, Improvement

*Electronic address: `alexand@ucy.ac.cy,marthac@temple.edu,haris@ucy.ac.cy`

I. INTRODUCTION

Over the last years, simulations of Quantum Chromodynamics (QCD) have advanced remarkably and are, nowadays, being carried out at close-to-physical values for the parameters of the theory. Therefore, *ab initio* calculations of hadron structure within lattice QCD yield results that can be connected to experiment more reliably than ever before. A number of lattice groups are producing results on nucleon form factors and first moments of structure functions at or close to the physical regime both in terms of pion mass as well as in terms of the continuum limit (see Ref. [1] and references therein). At the same time properties of other hadrons that are difficult to study experimentally are being pursued within lattice QCD. These include the axial charges of resonances such as the Δ [2] or other nucleon excited states [3], hyperons [4–6] and charm baryons [6]. For all these quantities, one needs the renormalization functions in order to obtain the continuum predictions. Moments of generalized parton distributions (GPDs) are connected to generalized form factors and provide detailed information on the internal structure of hadrons in terms of both the longitudinal momentum fraction and the total momentum transfer squared. Beyond the information that the form factors yield, such as size, magnetization and shape, GPDs encode additional information, relevant for experimental investigations, such as the decomposition of the total hadron spin into angular momentum and spin carried by quarks and gluons. In lattice QCD one calculates matrix elements of fermion operators between the relevant hadron states and unless these operators correspond to a conserved current they must be renormalized in order to extract the physical information one is after. In many cases, calculation of renormalization functions (RFs) can be carried out using lattice perturbation theory, which proves to be extremely helpful in cases where there is a mixing with operators of equal or lower dimension, such as the chromomagnetic operator [7, 8] and the operator measuring the glue of the nucleon [9, 10]. However, perturbation theory is reliable for a limited range of values of the coupling constant, g, and of the renormalization scale, μ. For this reason, a non-perturbative computation on the RFs is preferable.

In this work we will combine both perturbative and non-perturbative computations in order to obtain an improved evaluation for the RFs of the quark field, ultra-local and one-derivative fermion operators within the twisted mass formulation of Wilson lattice QCD [11]. In particular, we compute lattice artifacts to all orders in the lattice spacing, a, using one-loop perturbation theory and we subtract them from the non-perturbative results for the RFs. This subtraction suppresses lattice artifacts considerably depending on the operator under study and leads to a more accurate determination of the renormalization functions. We show that lattice artifacts are non-negligible in most cases, and are significantly larger than statistical errors.

We use the Rome-Southampton method (RI$'$ scheme) [12] to compute the renormalization coefficients of arbitrary quark-antiquark operators non-perturbatively. In this approach the renormalization conditions are defined similarly in perturbative and non-perturbative calculations. The RFs are obtained for different values of the renormalization scale, and on several ensembles corresponding to different pion masses, so that the chiral limit can be safely taken. Since the goal is to make contact with phenomenological and experimental studies, which almost exclusively refer to operators renormalized in the $\overline{\rm MS}$ scheme, one needs the renormalization functions leading from the bare operators on the lattice to the $\overline{\rm MS}$ operators in the continuum. The conversion to the $\overline{\rm MS}$ and the evolution to a reference scale of 2 GeV is performed using three-loop perturbation theory. An alternative procedure that has been under investication is the use of the RI/SMOM scheme [13] which has a non-exceptional, symmetric subtraction point. Such a scheme is expected to have infrared improved kinematics with suppressed non-perturbative affects. However, the synergy of our perturbative and non-perturbative procedures quaranties elimination of the lattice artifacts to a large extent.

The paper is organized as follows: Section II presents the lattice formulation and gives details on the gauge configurations and the parameters of each ensemble. Section II includes the definition of the operators under study, as well as the renormalization conditions for the RI$'$ scheme. The methodolody of the non-perturbative computation is described in Section III. Section IV focuses on the perturbative procedure for the evaluation of the one-loop lattice artifacts to all orders in the lattice spacing denoted by $\mathcal{O}(g^2\, a^\infty)$. This is a crucial component of this work, since the subtraction of the $\mathcal{O}(g^2\, a^\infty)$ contributions from the non-perturbative estimates of the RFs leads to removal of the bulk of lattice artifacts. The main part of the paper is Section V, which presents the results of this work, including their chiral extrapolation, the conversion to the $\overline{\rm MS}$ scheme and the evolution to a reference scale of 2 GeV, via the intermediate Renormalization Group Invariant scheme. Particular focus is given to the $\mathcal{O}(g^2\, a^\infty)$-corrected data for the RFs, and we show, for selected cases, a comparison with the $\mathcal{O}(g^2\, a^2)$-corrected expressions. The final values of the chirally extrapolated RFs at the limit $(a\, p)^2 \to 0$ are presented in Table III. In Section VII we give our conclusions. For completeness we provide in Appendix A all necessary formulae for the conversion to the $\overline{\rm MS}$ scheme, and in Appendix B we present the $\mathcal{O}(g^2\, a^\infty)$-corrected RFs for all the previous twisted mass fermions ensembles [14, 15], recomputed in the framework of this work.

II. FORMULATION

A. Simulation details

The gauge field configurations were generated by the European Twisted Mass Collaboration (ETMC) employing the twisted mass fermion action. We use ensembles generated with N_f=4 light degenerate quarks [16] with the twisted mass action, as well as N_f=2 degenerate quarks [17], in which a clover term is also included in the fermion action with $c_{\rm sw}$=1.57551. We note that the renormalization functions computed using the N_f=4 ensembles will be applied to renormalize matrix elements computed using N_f=2+1+1 gauge field configurations [18]. We adopt the RI$'$ renormalization scheme, which is mass independent, and consequently the RFs are defined at zero quark mass. For this reason, the N_f=2+1+1 ensembles cannot be used to compute the RFs due to the fact that the mass of the strange and charm quarks are fixed to their physical values, and extrapolation to the chiral limit is not possible. Therefore, in order to compute the renormalization functions needed to obtain physical observables, ETMC has generated N_f=4 ensembles at the same values of β so that the chiral limit can be taken. Details on the simulations can be found in Refs. [17, 19].

Automatic $\mathcal{O}(a)$ improvement for twisted mass fermions may be achieved with maximal twist, by tuning the $m_{\rm PCAC}$ quark mass to zero. For the case of N_f=4 configurations, achieving maximal twist is difficult particularly if the lattice spacing is not very fine, which is associated with a change in the slope of $m_{\rm PCAC}$ with respect to $1/(2\kappa)$ [20]. In order to tackle this issue, Monte Carlo simulations are performed in pairs not exactly at maximal twist but with opposite values of $m_{\rm PCAC}$. As proposed in Ref. [21], by averaging the RFs computed on ensembles with opposite values of $m_{\rm PCAC}$, $\mathcal{O}(a)$ improvement is achieved (see also Ref. [22] and references therein).

In the gluon sector we use, for all ensembles, the Iwasaki improved gauge action [23], which includes besides the plaquette term $U^{1\times1}_{x,\mu,\nu}$ also rectangular (1×2) Wilson loops $U^{1\times2}_{x,\mu,\nu}$

$$S_g = \frac{\beta}{3}\sum_x \left(b_0 \sum_{\substack{\mu,\nu=1\\ \mu<\nu}}^{4} \left\{1-\mathrm{Re\,Tr}(U^{1\times1}_{x,\mu,\nu})\right\} + b_1 \sum_{\substack{\mu,\nu=1\\ \mu\neq\nu}}^{4} \left\{1-\mathrm{Re\,Tr}(U^{1\times2}_{x,\mu,\nu})\right\}\right) \tag{1}$$

with β=$2\,N_c/g_0^2$, $b_1=-0.331$ and the (proper) normalization condition $b_0=1-8b_1=3.648$.

The simulation details, the parameters and the values of the pion mass [24] of each ensemble used in this work are given in Tables I - II, for the N_f=2 and N_f= 4 ensembles, respectively. The values of the lattice spacing have been determined using the nucleon mass [18, 25].

$a\mu$	κ	aM_{PS}	lattice size
$\beta=2.10$, $a=0.093$ fm, $c_{\rm sw}=1.57551$			
0.0009	0.13729	0.0621(2)	$48^3\times96$
0.0030	0.1373	0.110(4)	$24^3\times48$
0.0060	0.1373	0.160(4)	$24^3\times48$

TABLE I: Simulation details for the N_f=2 twisted mass ensembles with a clover term. The lattice spacing is determined using the nuleon mass computed using the same N_f=2 ensembles.

The number of configurations in each ensemble varies between 10 to 50 separated by 20-100 trajectories, depending on the ensemble. The small size of these ensembles, is more than sufficient for use of the momentum source method, which offers high statistical accuracy, easily below 0.5% even for 10 configurations (see Section III). In our computation, we mostly use "democratic momenta" in the spatial direction, such as:

$$(a\,p) \equiv 2\pi\left(\frac{n_t}{L_t}+\frac{1}{2\,L_t},\frac{n_x}{L_s},\frac{n_x}{L_s},\frac{n_x}{L_s}\right), \tag{2}$$

where L_t (L_s) is the temporal (spatial) extent of the lattice and n_t and n_x take values within the range:

$$n_t\,\epsilon\,[2,20]\,,\quad n_x\,\epsilon\,[1,10]\,, \tag{3}$$

depending on the lattice size of each ensemble, so that they correspond to momentum up to $(a\,p)^2\sim7$. To fill in some gaps between the momentum ranges we also include a few non-democratic momenta of the form $(n_t,n_x,n_x,n_x\pm1)$, which show similar behaviour with neighbouring democratic momenta. Alternatively, one can consider using twisted boundary conditions [26].

$a\mu$	κ	$a\mu^{sea}_{\rm PCAC}$	aM_{PS}	lattice size
		$\beta = 1.90$, $a = 0.0934$ fm		
0.0080	0.162689	+0.0275(4)	0.280(1)	$24^3 \times 48$
	0.163476	−0.0273(2)	0.227(1)	
0.0080	0.162876	+0.0398(1)	0.279(2)	$24^3 \times 48$
	0.163206	−0.0390(1)	0.241(1)	
		$\beta = 1.95$, $a = 0.082$ fm		
0.0020	0.160524	+0.0363(1)		$24^3 \times 48$
	0.161585	−0.0363(1)		
0.0085	0.160826	+0.0191(2)	0.277(2)	$24^3 \times 48$
	0.161229	−0.0209(2)	0.259(1)	
0.0180	0.160826	+0.0163(2)	0.317(1)	$24^3 \times 48$
	0.161229	−0.0160(2)	0.292(1)	
		$\beta = 2.10$, $a = 0.064$ fm		
0.0030	0.156042	+0.0042(1)	0.127(2)	$32^3 \times 64$
	0.156157	−0.0040(1)	0.129(3)	
0.0046	0.156017	+0.0056(1)	0.150(2)	$32^3 \times 64$
	0.156209	−0.0059(1)	0.160(4)	
0.0064	0.155983	+0.0069(1)	0.171(1)	$32^3 \times 64$
	0.156250	−0.0068(1)	0.180(4)	
0.0078	0.155949	+0.0082(1)	0.188(1)	$32^3 \times 64$
	0.156291	−0.0082(1)	0.191(3)	

TABLE II: Simulation details for the N_f=4 ensembles of twisted mass fermions. The lattice spacing is determined using the nucleon mass computed with N_f=2+1+1 twisted mass configurations at the same values of β.

B. Definition of operators and renormalization prescription

In this work we consider ultra-local fermion operators:

$$\mathcal{O}^a_S = \bar\chi\tau^a\chi = \begin{cases} \bar\psi\tau^a\psi & a=1,2 \\ -i\bar\psi\gamma_5\mathbb{1}\psi & a=3 \end{cases} \tag{4}$$

$$\mathcal{O}^a_P = \bar\chi\gamma_5\tau^a\chi = \begin{cases} \bar\psi\gamma_5\tau^a\psi & a=1,2 \\ -i\bar\psi\mathbb{1}\psi & a=3 \end{cases} \tag{5}$$

$$\mathcal{O}^a_V = \bar\chi\gamma_\mu\tau^a\chi = \begin{cases} \bar\psi\gamma_5\gamma_\mu\tau^2\psi & a=1 \\ -\bar\psi\gamma_5\gamma_\mu\tau^1\psi & a=2 \\ \bar\psi\gamma_\mu\tau^3\psi & a=3 \end{cases} \tag{6}$$

$$\mathcal{O}^a_A = \bar\chi\gamma_5\gamma_\mu\tau^a\chi = \begin{cases} \bar\psi\gamma_\mu\tau^2\psi & a=1 \\ -\bar\psi\gamma_\mu\tau^1\psi & a=2 \\ \bar\psi\gamma_5\gamma_\mu\tau^3\psi & a=3 \end{cases} \tag{7}$$

$$\mathcal{O}^a_T = \bar\chi\sigma_{\mu\nu}\tau^a\chi = \begin{cases} \bar\psi\sigma_{\mu\nu}\tau^a\psi & a=1,2 \\ -i\bar\psi\gamma_5\sigma_{\mu\nu}\mathbb{1}\psi & a=3 \end{cases} \tag{8}$$

$$\mathcal{O}^a_{Tp} = \bar\chi\gamma_5\sigma_{\mu\nu}\tau^a\chi = \begin{cases} \bar\psi\gamma_5\sigma_{\mu\nu}\tau^a\psi & a=1,2 \\ -i\bar\psi\sigma_{\mu\nu}\mathbb{1}\psi & a=3 \end{cases} \tag{9}$$

and the following one-derivative fermion operators:

$$\mathcal{O}^{\{\mu\,\nu\}}_{\rm DV} \quad = \overline{\chi}\gamma_{\{\mu}\overleftrightarrow{D}_{\nu\}}\tau^a\chi \quad = \begin{cases} \overline{\psi}\gamma_5\gamma_{\{\mu}\overleftrightarrow{D}_{\nu\}}\tau^2\psi & a=1 \\ -\overline{\psi}\gamma_5\gamma_{\{\mu}\overleftrightarrow{D}_{\nu\}}\tau^1\psi & a=2 \\ \overline{\psi}\gamma_{\{\mu}\overleftrightarrow{D}_{\nu\}}\tau^3\psi & a=3 \end{cases} \tag{10}$$

$$\mathcal{O}^{\{\mu\,\nu\}}_{\rm DA} \quad = \overline{\chi}\gamma_5\gamma_{\{\mu}\overleftrightarrow{D}_{\nu\}}\tau^a\chi \quad = \begin{cases} \overline{\psi}\gamma_{\{\mu}\overleftrightarrow{D}_{\nu\}}\tau^2\psi & a=1 \\ -\overline{\psi}\gamma_{\{\mu}\overleftrightarrow{D}_{\nu\}}\tau^1\psi & a=2 \\ \overline{\psi}\gamma_5\gamma_{\{\mu}\overleftrightarrow{D}_{\nu\}}\tau^3\psi & a=3 \end{cases} \tag{11}$$

$$\mathcal{O}^{\mu\,\{\nu\,\rho\}}_{\rm DT} \quad = \overline{\chi}\gamma_5\sigma_{\mu\{\nu}\overleftrightarrow{D}_{\rho\}}\tau^a\chi \quad = \begin{cases} \overline{\psi}\gamma_5\sigma_{\mu\{\nu}\overleftrightarrow{D}_{\rho\}}\tau^a\psi & a=1,2 \\ -i\,\overline{\psi}\sigma_{\mu\{\nu}\overleftrightarrow{D}_{\rho\}}1\!\!1\psi & a=3 \end{cases}, \tag{12}$$

all given in the twisted and physical basis as shown above. The covariant derivative is defined as:

$$\overleftrightarrow{D} \; = \frac{1}{2}\Big[\frac{(\overrightarrow{\nabla}_\mu + \overrightarrow{\nabla}^*_\mu)}{2} - \frac{(\overleftarrow{\nabla}_\mu + \overleftarrow{\nabla}^*_\mu)}{2}\Big] \tag{13}$$

where

$$\overrightarrow{\nabla}_\mu\psi(x) = \frac{1}{a}\Big[U_\mu(x)\psi(x+a\hat{\mu}) - \psi(x)\Big] \quad \text{and} \quad \overrightarrow{\nabla}^*_\mu\psi(x) = -\frac{1}{a}\Big[U^\dagger_\mu(x-a\hat{\mu})\psi(x-a\hat{\mu}) - \psi(x)\Big] \tag{14}$$

and

$$\overline{\psi}(x)\overleftarrow{\nabla}_\mu = \frac{1}{a}\Big[\overline{\psi}(x+a\hat{\mu})U^\dagger_\mu(x) - \overline{\psi}(x)\Big] \quad \text{and} \quad \overline{\psi}(x)\overleftarrow{\nabla}^*_\mu = -\frac{1}{a}\Big[\overline{\psi}(x-a\hat{\mu})U_\mu(x-a\hat{\mu}) - \overline{\psi}(x)\Big] \quad . \tag{15}$$

For completeness we include in the list $\mathcal{O}^a_{Tp}$ even though its components are related to those of $\mathcal{O}^a_T$. We denote the corresponding RFs of the ultra-local fermion bilinears by $Z^a_{\rm S}$, $Z^a_{\rm P}$, $Z^a_{\rm V}$, $Z^a_{\rm A}$, $Z^a_{\rm T}$, $Z^a_{\rm Tp}$. In a massless renormalization scheme, such as the RI$'$, the RFs are defined in the chiral limit, where iso-spin symmetry is recovered. Hence, the renormalization functions become independent of the isospin index $a=1,2,3$ and we drop the a index from here on. Still note that, for instance, the physical $\bar{\psi}\gamma_\mu\tau^1\psi$ is renormalized with $Z_{\rm A}$ while $\bar{\psi}\gamma_\mu\tau^3\psi$ needs $Z_{\rm V}$, which differ from each other even in the chiral limit.

The one-derivative operators are symmetrized over two Lorentz indices and are made traceless:

$$\mathcal{O}^{\{\sigma\,\tau\}} \equiv \frac{1}{2}\Big(\mathcal{O}^{\sigma\,\tau} + \mathcal{O}^{\tau\,\sigma}\Big) - \frac{1}{4}\delta^{\sigma\,\tau}\sum_\lambda \mathcal{O}^{\lambda\,\lambda}\,, \tag{16}$$

which avoids mixing with lower dimension operators. The corresponding RFs of the one-derivative operators are denoted by $Z^a_{\rm DV}$, $Z^a_{\rm DA}$, $Z^a_{\rm DT}$. The one-derivative operators fall into different irreducible representations of the hypercubic group, depending on the choice of indices. Hence, we distinguish among them according to the following

$$\mathcal{O}_{\rm DV1} \; = \; \mathcal{O}_{\rm DV} \text{ with } \mu=\nu \tag{17}$$
$$\mathcal{O}_{\rm DV2} \; = \; \mathcal{O}_{\rm DV} \text{ with } \mu\neq\nu \tag{18}$$
$$\mathcal{O}_{\rm DA1} \; = \; \mathcal{O}_{\rm DA} \text{ with } \mu=\nu \tag{19}$$
$$\mathcal{O}_{\rm DA2} \; = \; \mathcal{O}_{\rm DA} \text{ with } \mu\neq\nu \tag{20}$$
$$\mathcal{O}_{\rm DT1} \; = \; \mathcal{O}_{\rm DT} \text{ with } \mu\neq\nu=\rho \tag{21}$$
$$\mathcal{O}_{\rm DT2} \; = \; \mathcal{O}_{\rm DT} \text{ with } \mu\neq\nu\neq\rho\neq\mu\,. \tag{22}$$

Thus, $Z_{\rm DV1}$ will be different from $Z_{\rm DV2}$, but renormalized matrix elements of the two corresponding operators will be components of the same tensor in the continuum limit.

The renormalization functions are computed in the RI$'$ scheme at different renormalization scales, μ. The RFs are determined by imposing the following conditions:

$$Z_{\rm q} = \frac{1}{12}{\rm Tr}\left[(S^L(p))^{-1}\, S^{\rm Born}(p)\right]\Big|_{p^2=\mu^2} \tag{23}$$

$$Z_{\rm q}^{-1}\, Z_{\mathcal{O}}\, \frac{1}{12}{\rm Tr}\left[\Gamma^L(p)\, \Gamma^{\rm Born-1}(p)\right]\Big|_{p^2=\mu^2} \;=\; 1\,, \tag{24}$$

where the momentum p is set to the renormalization scale μ. The trace is taken over spin and color indices, $S^{\rm Born}$ is the tree-level result for the propagator, and $\Gamma^{\rm Born}$ is the tree-level expressions for the fermion operators, that is

$$\Gamma^{\rm Born}(p) = 1\!\!1,\ \gamma_5,\ \gamma_\mu,\ \gamma_5\,\gamma_\mu,\ \gamma_5\,\sigma_{\mu\nu},\ \sigma_{\mu\nu} \tag{25}$$

for the ultra-local bilinears, and

$$\mathcal{O}_{\rm DV}^{\{\mu\nu\}} \;=\; \frac{1}{2}\Big[\overline{\Psi}\,\gamma_\mu\, \overleftrightarrow{D}_\nu\,\Psi + \overline{\Psi}\,\gamma_\nu\, \overleftrightarrow{D}_\mu\,\Psi\Big] - \frac{1}{4}\delta_{\mu\nu}\sum_\tau \overline{\Psi}\,\gamma_\tau\, \overleftrightarrow{D}_\tau\,\Psi \tag{26}$$

$$\mathcal{O}_{\rm DA}^{\{\mu\nu\}} \;=\; \frac{1}{2}\Big[\overline{\Psi}\,\gamma_5\gamma_\mu\, \overleftrightarrow{D}_\nu\,\Psi + \overline{\Psi}\,\gamma_5\gamma_\nu\, \overleftrightarrow{D}_\mu\,\Psi\Big] - \frac{1}{4}\delta_{\mu\nu}\sum_\tau \overline{\Psi}\,\gamma_5\gamma_\tau\, \overleftrightarrow{D}_\tau\,\Psi \tag{27}$$

$$\mathcal{O}_{\rm DT}^{\mu\{\nu\rho\}} \;=\; \frac{1}{2}\Big[\overline{\Psi}\,\gamma_5\sigma_{\mu\nu}\, \overleftrightarrow{D}_\rho\,\Psi + \overline{\Psi}\,\gamma_5\sigma_{\mu\rho}\, \overleftrightarrow{D}_\nu\,\Psi\Big] - \frac{1}{4}\delta_{\nu\rho}\sum_\tau \overline{\Psi}\,\gamma_5\sigma_{\mu\tau}\, \overleftrightarrow{D}_\tau\,\Psi \tag{28}$$

for the one-derivative operators. The presence of $S^{\rm Born}$ and $\Gamma^{\rm Born}$ ensure that $Z_{\rm q}=1$, $Z_{\mathcal{O}}=1$ when the gauge field is set to unity. The RI$'$ values for the RFs are translated to the $\overline{\rm MS}$ scheme at μ =2 GeV using an intermediate Renormalization Group Invariant scheme.

III. NON-PERTURBATIVE CALCULATION

For the non-perturbative evaluation we follow the same procedure as our previous work [14, 15], and here we summarize the important steps of the calculation. We first write the operators in the form

$$\mathcal{O}(z) = \sum_{z'} \overline{u}(z)\mathcal{J}(z,z')d(z')\,, \tag{29}$$

where u and d denote quark fields in the physical basis and $\mathcal{J}$ denotes the operator we are interested in. For example $\mathcal{J}(z,z') = \delta_{z,z'}\gamma_\mu$ corresponds to the local vector current. For each operator we define a bare vertex function given by

$$G(p) = \frac{a^{12}}{V}\sum_{x,y,z,z'} e^{-ip(x-y)}\langle u(x)\overline{u}(z)\mathcal{J}(z,z')d(z')\overline{d}(y)\rangle\,, \tag{30}$$

where p is a momentum allowed by the boundary conditions, V is the lattice volume, and the gauge average, denoted by the brackets, is performed over gauge-fixed configurations. The Dirac and color indices of $G(p)$ are suppressed for simplicity.

We employ the approach, introduced in Ref. [27], which uses directly Eq. (30) without employing translation invariance [1], and one must now use a source that is momentum dependent but can couple to any operator. For twisted mass fermions, we use the symmetry $S^u(x,y) = \gamma_5 S^{d\dagger}(y,x)\gamma_5$ between the $u-$ and $d-$quark propagators, and therefore, with a single inversion one can extract the vertex function for a single momentum. The advantage of the momentum source approach is a high statistical accuracy and the evaluation of the vertex for any operator at no significant additional computational cost. The drawback is that we need a new inversion for each momentum. We

[1] In an alternative approach that relies on translation invariance, one may shift the coordinates of the correlators in Eq. (30) to position $z=0$ [22].

fix to Landau gauge using a stochastic over-relaxation algorithm [28], converging to a gauge transformation which minimizes the functional

$$F = \sum_{x,\mu} \mathrm{Re}\ \mathrm{tr}\left[U_\mu(x) + U^\dagger_\mu(x-\hat{\mu})\right] \ . \tag{31}$$

The propagator in momentum space, in the physical basis, is defined by

$$S^u(p) = \frac{a^8}{V}\sum_{x,y} e^{-ip(x-y)} \left\langle u(x)\overline{u}(y)\right\rangle \ , \qquad S^d(p) = \frac{a^8}{V}\sum_{x,y} e^{-ip(x-y)} \left\langle d(x)\overline{d}(y)\right\rangle \ , \tag{32}$$

and an amputated vertex function is given by

$$\Gamma(p) = (S^u(p))^{-1}\, G(p)\, (S^d(p))^{-1} \, . \tag{33}$$

Finally, the corresponding renormalized quantities are assigned the values

$$S_R(p) = Z_{\rm q} S(p)\, , \qquad\qquad \Gamma_R(p) = Z_{\rm q}^{-1} Z_{\mathcal{O}} \Gamma(p) \quad . \tag{34}$$

In the twisted basis at maximal twist, Eq. (30) takes the form

$$G(p) = \frac{a^{12}}{4V} \sum_{x,y,z,z'} e^{-ip(x-y)} \left\langle (\mathbb{1}+i\gamma_5)u(x)\overline{u}(z)(\mathbb{1}+i\gamma_5)\mathcal{J}(z,z')(\mathbb{1}-i\gamma_5)d(z')\, \overline{d}(y)(\mathbb{1}-i\gamma_5)\right\rangle \ , \tag{35}$$

which simplifies when using the relation between the u- and d-quark propagators, that is $\mathcal{S}^u(x,z) = \gamma_5 {\mathcal{S}^d}^\dagger(z,x)\gamma_5$. After integration over the fermion fields it becomes

$$G(p) = -\frac{a^{12}}{4V}\sum_{z,\, z'} \left\langle (\mathbb{1}-i\gamma_5){\breve{\mathcal{S}}^d}{}^\dagger(z,p)(\mathbb{1}-i\gamma_5)\mathcal{J}(z,z')(\mathbb{1}-i\gamma_5)\breve{\mathcal{S}}^d(z',p)(\mathbb{1}-i\gamma_5)\right\rangle^G \ , \tag{36}$$

where $\langle ...\rangle^G$ denotes the integration over gluon fields, and $\breve{\mathcal{S}}(z,p) = \sum_y e^{ipy}\mathcal{S}(z,y)$ is the Fourier transformed propagator with respect to one of its arguments, on a particular gauge background. It can be obtained by inversion using the Fourier source

$$b^a_\alpha(x) = e^{ipx}\delta_{\alpha\beta}\delta_{ab}\, , \tag{37}$$

for all Dirac α and color a indices. The propagators in the physical basis given in Eq. (32) can be obtained from

$$\begin{aligned} S^d(p) &= \frac{1}{4}\sum_z e^{-ipz}\langle(\mathbb{1}-i\gamma_5)\breve{\mathcal{S}}^d(z,p)(\mathbb{1}-i\gamma_5)\rangle^G \\ S^u(p) &= -\frac{1}{4}\sum_z e^{+ipz}\langle(\mathbb{1}-i\gamma_5){\breve{\mathcal{S}}^d}{}^\dagger(z,p)(\mathbb{1}-i\gamma_5)\rangle^G\, , \end{aligned} \tag{38}$$

which only need 12 inversions (instead of 24) despite the occurrence of both u and d quarks in the original expression. We evaluate Eq. (35) and Eq. (38) for each momentum separately employing Fourier sources over a range of $(a\,p)^2$ for which perturbative results can be trusted and finite a corrections are reasonably small. The amputated vertex functions of Eq. (33) computed for each operator, as well as the inverse quark propagator, enter the renormalization prescription of Eqs. (23) - (24).

IV. ONE-LOOP CALCULATION OF ARTIFACTS TO ALL ORDERS IN THE LATTICE SPACING

An improvement over previous work [14, 15], where we evaluated the $\mathcal{O}(g^2\, a^2)$ perturbative artifacts, is the computation of the one-loop perturbative artifacts to all orders in the lattice spacing, $\mathcal{O}(g^2\, a^\infty)$. These artifacts are unavoidably present in the non-perturbative vertex functions of the fermion propagator and fermion operators under study. In our previous work [14, 15], the $\mathcal{O}(g^2\, a^2)$ perturbative artifacts were subtracted from the non-perturbative RFs, leading to improved estimates. However, for large values of the scale $(a\,p)^2$, the $\mathcal{O}(g^2\, a^2)$ terms tend to increase becoming, thus, unreliable.

As will be demonstrated by our results, the lattice artifacts depend on the operator under study, as well as on several parameters such as the coupling constant, the fermion and gluon action parameters, the lattice size, the lattice spacing and the renormalization scale. Thus, a proper subtraction of the finite lattice size effects from the non-perturbative values requires a separate perturbative evaluation of the $\mathcal{O}(g^2\,a^\infty)$ terms for each ensemble and each value of the four-momentum, in order to match our non-perturbative computation. In other words, the $\mathcal{O}(g^2\,a^\infty)$ contributions that are subtracted from each black circle point shown in the plots of Section V requires a separate perturbative computation. Unlike the case of the $\mathcal{O}(g^2\,a^2)$-subtraction used in our previous work for the renormalization functions [14, 15, 29], the $\mathcal{O}(g^2\,a^\infty)$ contributions cannot be given in a closed form.

There are six Feynman diagrams that enter the perturbative computation: Two for the fermion propagator and four for the fermion operators, as shown in Figs. 1 - 2. The operator insersion is represented by a cross. In this work we restrict ourselves to forward matrix elements (i.e. 2-point Green's functions, zero momentum operator insertions). The Feynman diagrams are evaluated using our symbolic package in Mathematica, and details on the algebraic operations can be found in Ref. [29].

FIG. 1: One-loop diagrams contributing to the fermion propagator. Wavy (solid) lines represent gluons (fermions).

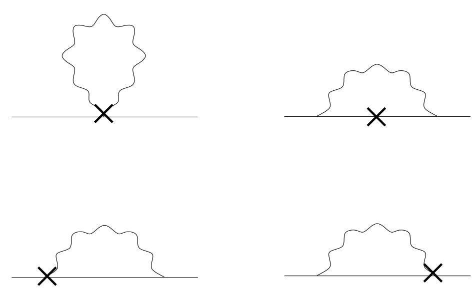

FIG. 2: One-loop diagrams contributing to the computation of the fermion operators. A wavy (solid) line represents gluons (fermions). A cross denotes an insertion of the operator under study. In the case of the ultra-local operators, only the upper right diagram contributes due to the absense of gluons in the vertices.

As a general strategy in our perturbative computations for the RFs we employ a variety of fermionic and gluonic actions, in order to obtain results that are applicable to simulations performed by various research groups. In this paper, however, we only present the results for the twisted mass action including a clover term. The latter is kept as a free parameter and can be sent to zero as required for the N_f=4 ensembles presented in Table II. Although the clover parameter is treated as free throughout the perturbative computation, for our final estimates in the N_f=2 ensembles it is set to its tree-level value suggested by one-loop perturbation theory, $c_{\rm sw}=1$.

The computation of the $\mathcal{O}(g^2\,a^\infty)$ terms was first employed by the QCDSF Collaboration [30, 31] for Clover fermions and Wilson gluons, and was later generalized to include more complicated fermion and gluon actions [32]. The main difference between the computation of the $\mathcal{O}(g^2\,a^\infty)$ and the $\mathcal{O}(g^2\,a^2)$ terms, is that the latter are extracted by performing a Taylor expansion with respect to a. The $\mathcal{O}(g^2\,a^\infty)$ terms, however, cannot be given in a closed form in terms of a (since it is included in the propagators) and a separate calculation is performed for each value of the momentum, $(a\,p)^2$. Of course, from the resulting expression one must omit the $\mathcal{O}(g^2\,a^0)$ terms since we are interested only in the lattice artifacts. Note that, in most cases, the latter contributions include logarithms ($\mathcal{O}(g^2\log(a))$), which are also subtracted. In a nutshell, the lattice artifacts to all orders in the lattice spacing are computed in the procedure summarized in the following expressions, in which the $\mathcal{O}(g^2\,a^0)$ terms computed in Ref. [29], are omitted:

$$D\mathcal{Z}_q(a,p) = \left(\mathcal{V}_q(a,p) - \mathcal{V}_q(0,p)\right)\Big|_{p^2=\mu^2} \tag{39}$$

$$D\mathcal{Z}_\mathcal{O}(a,p) = \left(\frac{\mathcal{V}_q(a,p)}{\mathcal{V}_\mathcal{O}(a,p)} - \frac{\mathcal{V}_q(0,p)}{\mathcal{V}_\mathcal{O}(0,p)}\right)\Big|_{p^2=\mu^2}\,, \tag{40}$$

where

$$\mathcal{V}_q(a,p) = \frac{1}{12}\mathrm{Tr}\left[(S^L(a,p))^{-1}\, S^{\mathrm{Born}}(p)\right] , \qquad \mathcal{V}_{\mathcal{O}}(a,p) = \frac{1}{12}\mathrm{Tr}\left[\Gamma^L(a,p)\, \Gamma^{\mathrm{Born}-1}(p)\right] \tag{41}$$

and $S^L(a,p)$, $\Gamma^L(a,p)$ are the results up to one loop and to all orders in a. Finally, the perturbative $\mathcal{O}(g^2 a^\infty)$-terms are subtracted form the non-perturbative values

$$Z_q^{\mathrm{RI}',\mathrm{sub}}(p,a) = Z_q^{\mathrm{RI}'}(p,a) - D\mathcal{Z}_q(a,p) \tag{42}$$

$$Z_{\mathcal{O}}^{\mathrm{RI}',\mathrm{sub}}(p,a) = Z_{\mathcal{O}}^{\mathrm{RI}'}(p,a) - D\mathcal{Z}_{\mathcal{O}}(a,p)\,. \tag{43}$$

In Figs. 3 - 8 we plot $D\mathcal{Z}_q(a,p)/g^2$ and $D\mathcal{Z}_{\mathcal{O}}(a,p)/g^2$ for the ultra-local bilinears corresponding to the Iwasaki improved action using a lattice size of $24^3\times 48$ and several values of $(a\,p)^2$ within the range of 0-4. For comparison we also include the corresponding $\mathcal{O}(g^2\,a^0)/g^2$ terms computed in Ref. [29]. Since a clover term is included in the $N_f{=}2$ ensembles, we consider both values: $c_{\mathrm{sw}} = 0$ (left figures) and $c_{\mathrm{sw}} = 1$ (right figures). An immediate observation is that momenta with the same $(a\,p)^2$ lead to different lattice artifacts, which is expected, since beyond $\mathcal{O}(a^0)$ these terms depend not only on the length, but also on the direction of the four-vector p, due to the presence of Lorentz noninvariant structures, such as:

$$a^2\,\frac{p4}{p2} \equiv \frac{\sum_\rho a^4 p_\rho^4}{\sum_\rho a^2 p_\rho^2}\,, \tag{44}$$

appearing to $\mathcal{O}(g^2a^2)$. It is also interesting to see that the lattice artifacts depend on the operator under study in a non-predictible way since in some cases (Z_{q}, Z_{V}, Z_{T}) the inclusion of a clover term diminishes the artifacts, while in another (Z_{S}) it enhances them. For the case of Z_{A} and Z_{P} the lattice artifacts for $c_{\mathrm{sw}} = 0, 1$ are comparable. As expected, comparison between $\mathcal{O}(g^2\,a^2)$ and $\mathcal{O}(g^2\,a^\infty)$ for small values of the momenta ($(a\,p)^2 \ll 1$) reveals a very good agreement, since the $\mathcal{O}(g^2\,a^2)$ terms are the leading contributions of the lattice artifacts. For larger momenta the difference between $\mathcal{O}(g^2\,a^2)$ and $\mathcal{O}(g^2\,a^\infty)$ is more apparent, as will be discussed in Section V.

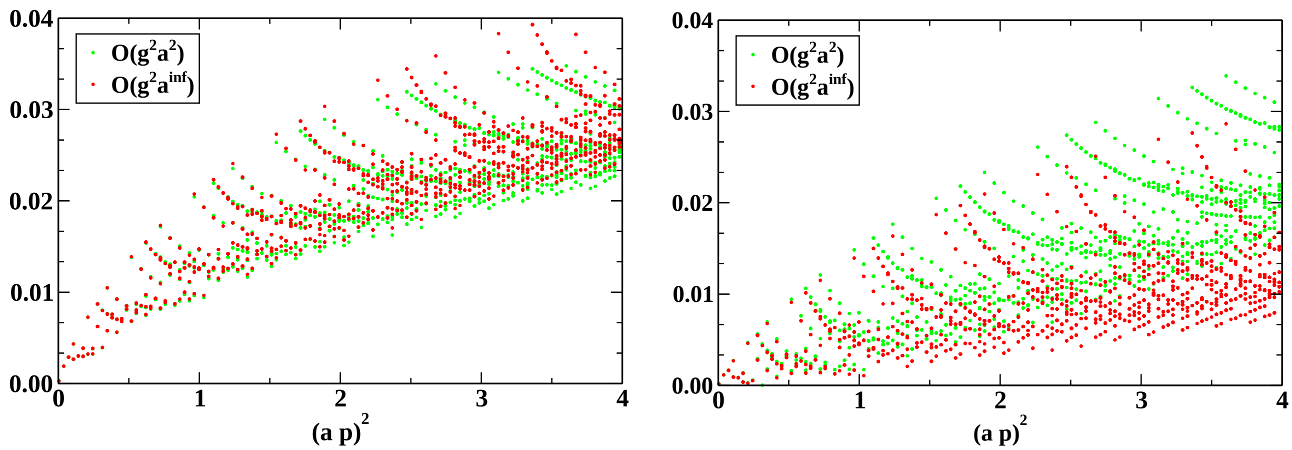

FIG. 3: $D\mathcal{Z}_q(a,p)/g^2$ as a function of $(a\,p)^2$ with the Iwasaki gluon action and a $24^3\times 48$ lattice for $c_{\mathrm{sw}} = 0$ (left) and $c_{\mathrm{sw}} = 1$ (right).

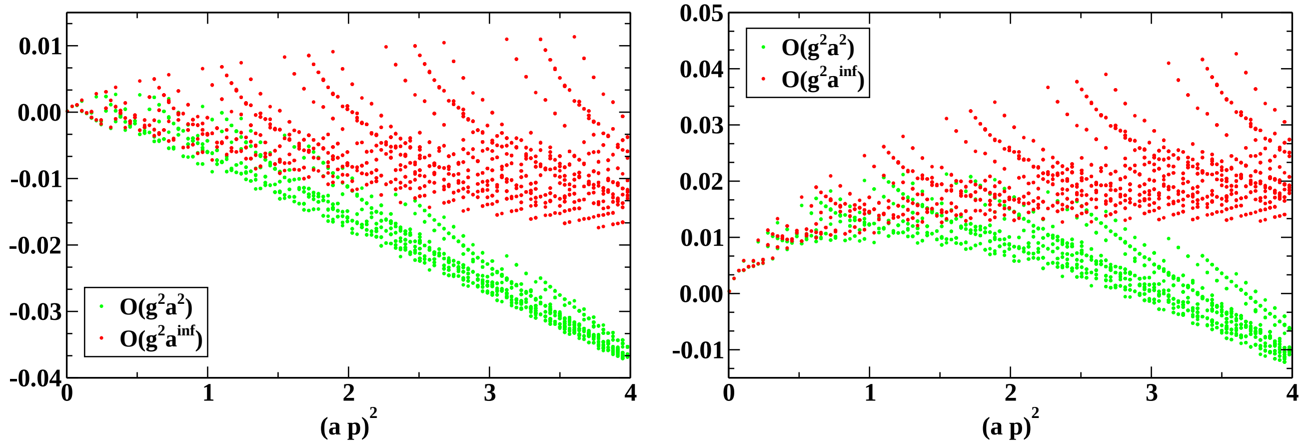

FIG. 4: $D\mathcal{Z}_S(a,p)/g^2$ as a function of $(a\,p)^2$. The notation is the same as for Fig. 3.

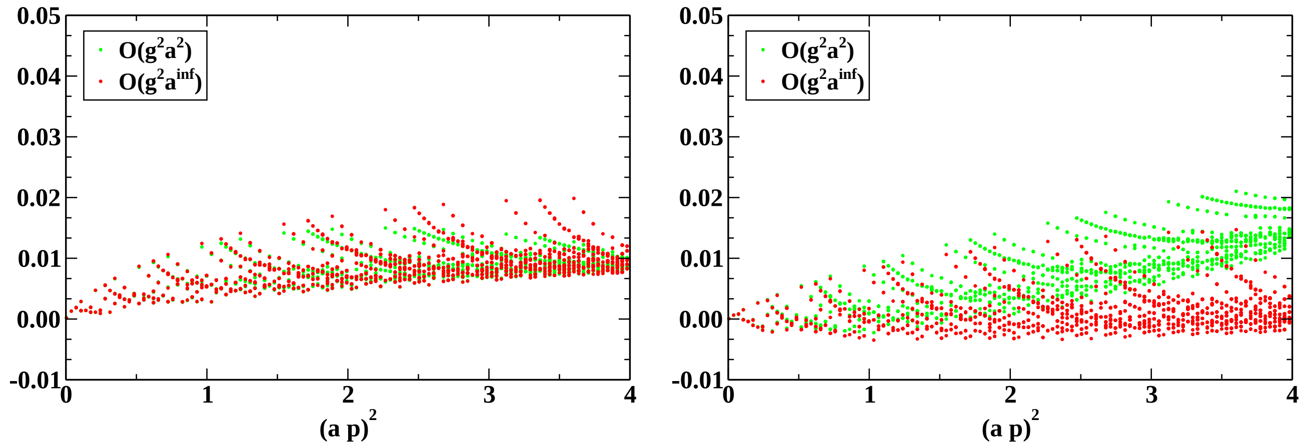

FIG. 5: $D\mathcal{Z}_P(a,p)/g^2$ as a function of $(a\,p)^2$. The notation is the same as for Fig. 3.

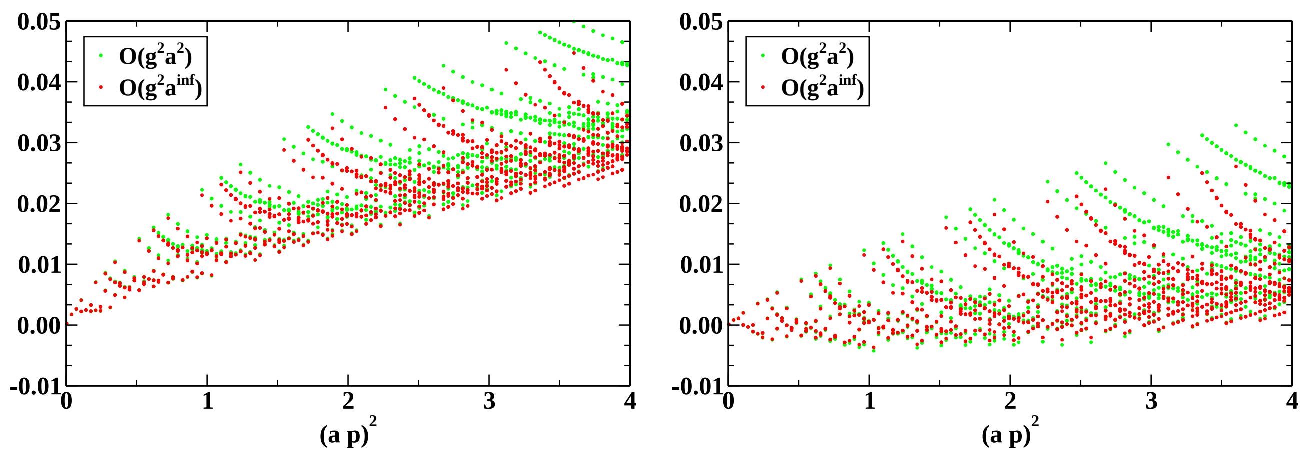

FIG. 6: $D\mathcal{Z}_V(a,p)/g^2$ as a function of $(a\,p)^2$. The notation is the same as for Fig. 3.

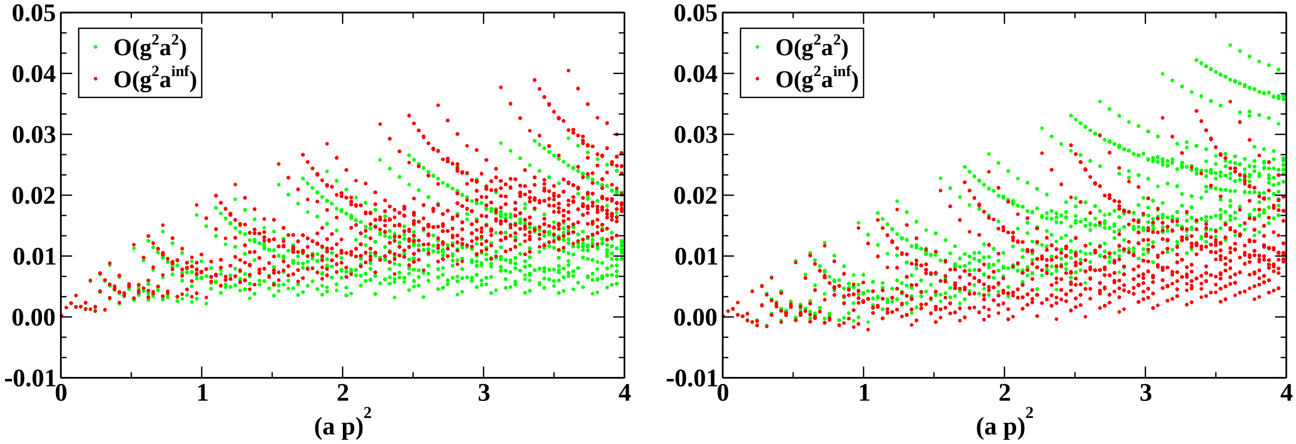

FIG. 7: $D\mathcal{Z}_A(a,p)/g^2$ as a function of $(a\,p)^2$. The notation is the same as for Fig. 3.

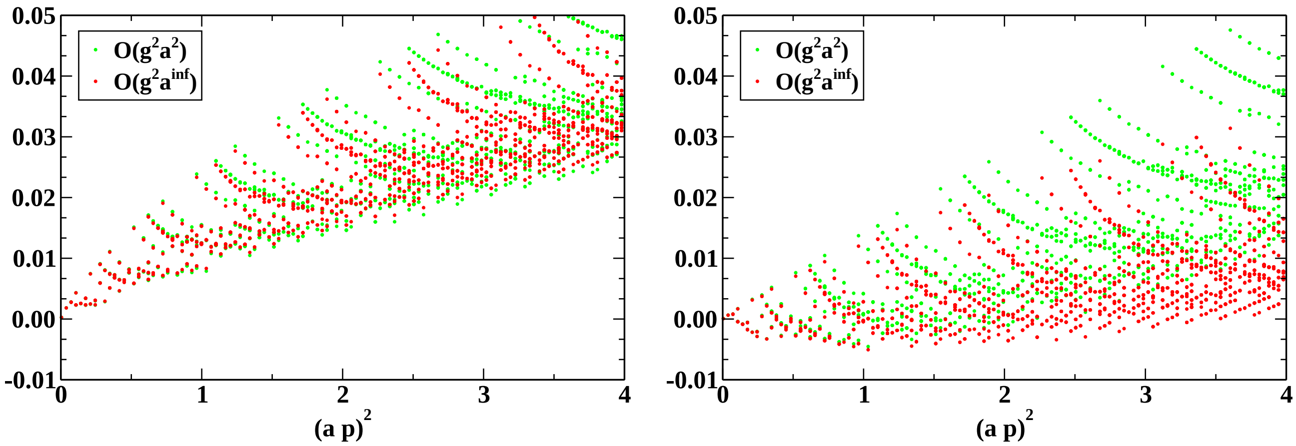

FIG. 8: $D\mathcal{Z}_T(a,p)/g^2$ as a function of $(a\,p)^2$. The notation is the same as for Fig. 3.

V. NON-PERTURBATIVE EVALUATION

A. Chiral extrapolation

In order to obtain the renormalization functions in the chiral limit we perform an extrapolation using a linear fit with respect to m_π^2. We find that the RFs obtained in this work have a very mild dependence on the pion mass for all ensembles. In fact, with the exception of a few small values of $(a\,p)^2$, there is no visible pion mass dependence within the small statistical errors. Allowing a slope and performing a linear extrapolation with respect to m_π^2 the data yield a slope consistent with zero. Figs. 9 - 12 demonstrate the pion mass dependence of the RFs using the N_f=2 and N_f=4 ensembles at β=2.10. The statistical errors are too small to be visible. Figs. 9 - 11 provide a more general picture of the m_π-dependence by displaying the RFs as a function of the renormalization scale ($\mu^2 = p^2$), while the two plots of Fig. 12 show the data at $(a\,p)^2 = 3$ as a function of the twisted mass $a\,\mu^{\rm sea}$. These plots show clearly that the slope of the fit is consistent with zero.

In this discussion the renormalization function of the pseudoscalar density, $Z_{\rm P}$, has been excluded since there is pion pole contamination that needs to be taken into account. Thus, a polynomial fit with respect to the pion mass is not suitable. An approriate chiral extrapolation of $Z_{\rm P}$ and the ratio $Z_{\rm P}/Z_{\rm S}$ is discussed in the following Subsection.

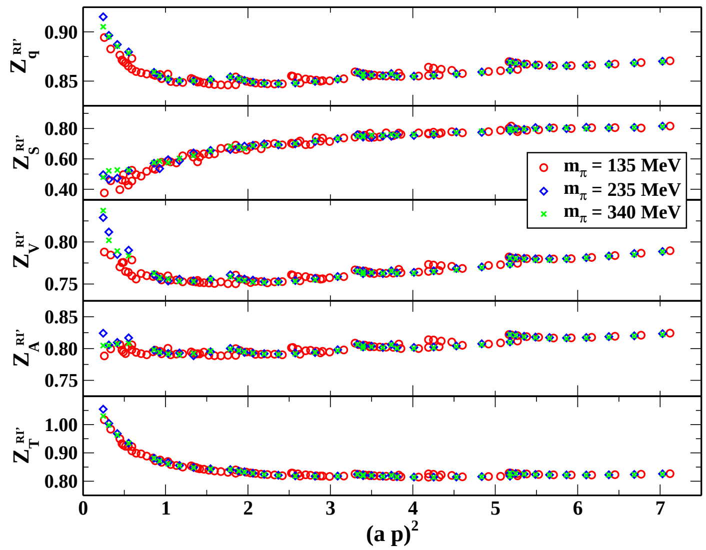

FIG. 9: Pion mass dependence of $Z_{\rm q}$ and the RFs of the ultra-local bilinears for N_f=2 at β=2.10 as a function of the renormalization scale.

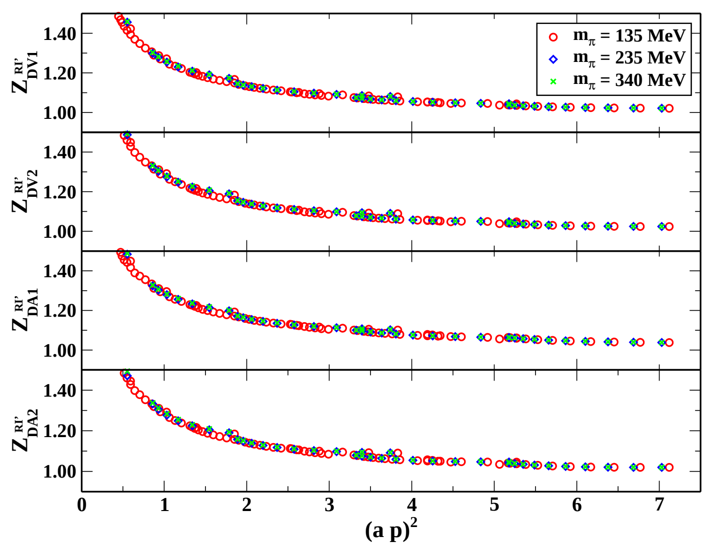

FIG. 10: Pion mass dependence of the RFs of the one-derivative vector and axial operators for N_f=2 at β=2.10 as a function of the renormalization scale.

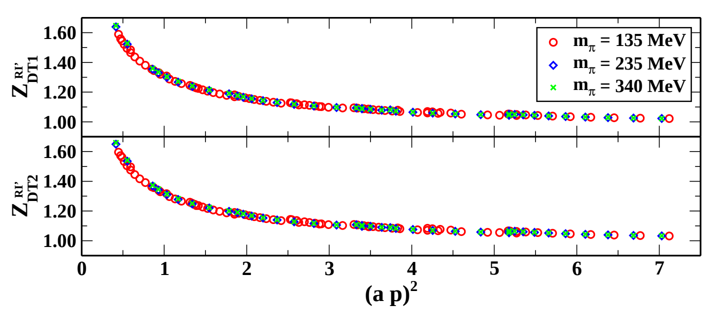

FIG. 11: Pion mass dependence of the RFs of the one-derivative tensor operator for N_f=2 at β=2.10 as a function of the renormalization scale.

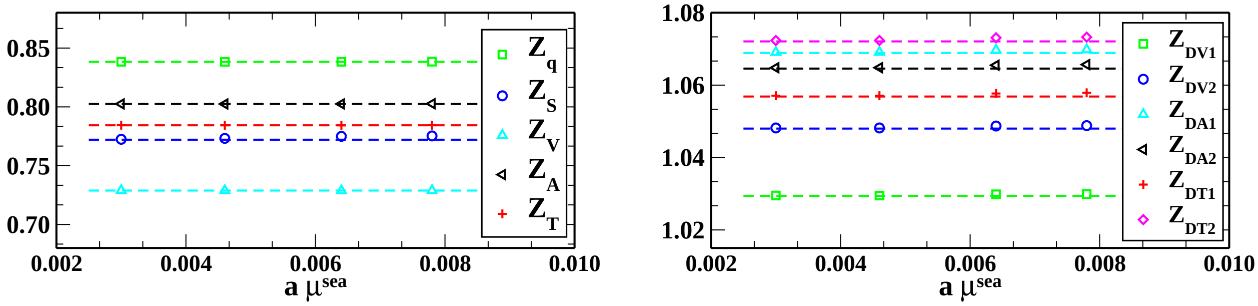

FIG. 12: Pion mass dependence of $Z_{\rm q}$ and the RFs of the ultra-local bilinears (left plot) and the one-derivative operators (right plot) for N_f=4 at β=2.10 as a function of $a\,\mu^{\rm sea}$ at $(a\,p)^2 = 3$.

B. Pion-pole subtraction of $Z_{\rm P}$ and $Z_{\rm P}/Z_{\rm S}$

The correlation functions of the pseudoscalar operator have pion-pole contamination which needs to be treated carefully. In order to subtract the pole contribution we use a 2- and 3-parameter Ansatz for the pseudoscalar amputated vertex function, Γ_P, of the form:

$$F_P^{(2)} \;=\; a_P + \frac{c_P}{m_\pi^2}\,, \tag{45}$$

$$F_P^{(3)} \;=\; a_P + b_P\, m_\pi^2 + \frac{c_P}{m_\pi^2}\,. \tag{46}$$

The fit parameters depend on both the momentum and the value of β (i.e. $a_P \equiv a_P(\beta, p)$), and thus we estimate them separately on each value of p and β. Similar to the case of SLiNC fermions we find that the coefficient b_P is very small and competes with c_P in the 3-parameter fit. In addition, they both carry large statistical errors, which result in a large error in the final determination of $Z_{\rm P}$ once the term c_P/m_π^2 is subtracted from the pseudoscalar matrix elements:

$$\Gamma_P^{\rm sub} = \Gamma_P - \frac{c_P}{m_\pi^2}. \tag{47}$$

A way around this problem is to employ the 2-parameter fit of Eq. (45) directly to the ratio:

$$V_P(p,\, m_\pi) = \frac{\Gamma_P(p,\, m_\pi)}{Z_{\rm q}(p,\, m_\pi)\, C_P^{{\rm RI}',\overline{\rm MS}}(p, 2\,{\rm GeV})}\,, \tag{48}$$

where $C_P^{{\rm RI}',\overline{\rm MS}}(p, 2\,{\rm GeV})$ is the conversion to the $\overline{\rm MS}$ scheme and the evolution to a scale of 2 GeV. The procedure we actually follow is to apply the 2-parameter fit (given in Eq. (45)) to the ratio of Eq. (48). This fit allows us to obtain directly $Z_{\rm P}^{\overline{\rm MS}}$ in the $\overline{\rm MS}$-scheme and at the chiral limit from the extracted parameter a_P via: $Z_{\rm P}^{\overline{\rm MS}} = 1/a_P$. [2] from $1/a_P$. In a similar manner, we obtain directly $Z_{\rm S}/Z_{\rm P}$ from the pion mass independent coefficient, a_P, computed by applying Eq. (45)

$$V_{SP}(p, m_\pi) = \frac{\Gamma_P(p, m_\pi)}{\Gamma_S(p, m_\pi)}\,. \tag{49}$$

As an example of the pion pole contamination and its subtraction we show, in Fig. 13, $V_P(p,\, m_\pi)$ and $V_{SP}(p,\, m_\pi)$ using the N_f=2 ensembles at β=2.10 for each value of the pion mass before and after the sutraction of the pion pole term, $\frac{c_P(p^2)}{m_\pi^2}$. Fig. 14 is similar to Fig. 13 for the N_f=4 and β=2.10 ensembles. The range of the y-axis is the same for the unsubtracted and subtracted cases in order to see clearly the effectiveness of the pion-pole subtraction.

---

[2] Alternative fit functions and their stability are discussed in Ref. [32].

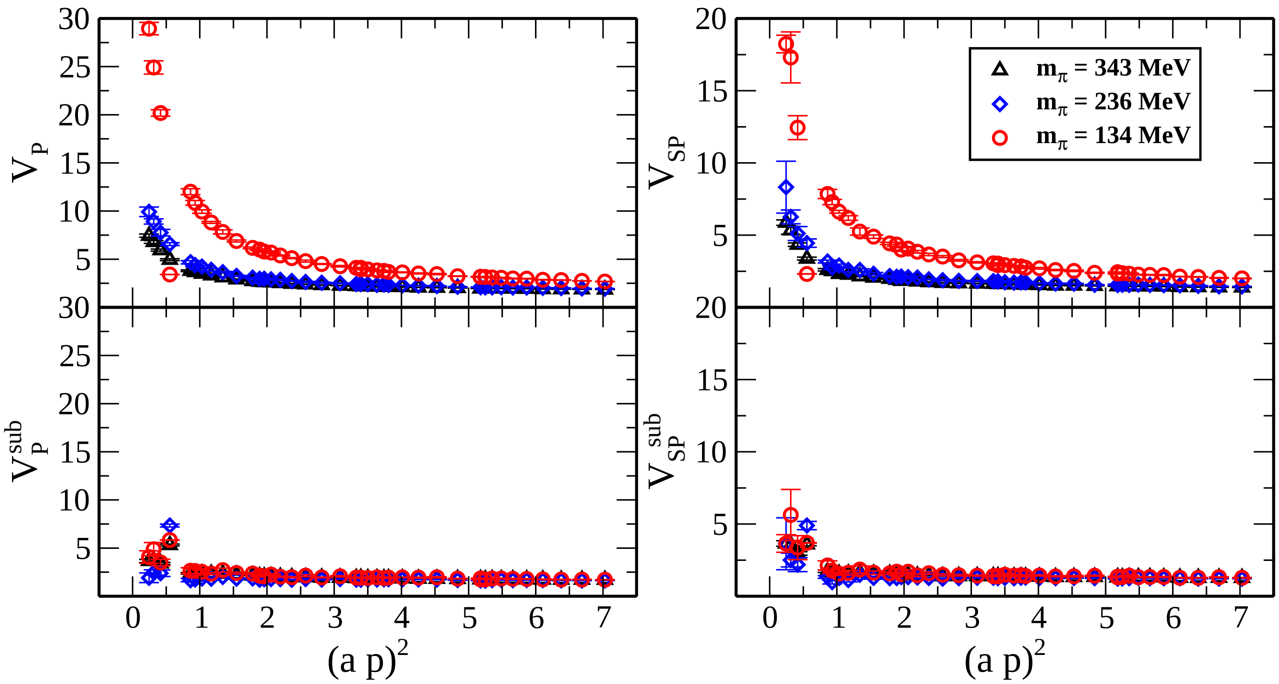

FIG. 13: Upper panels: Eq. (48) (left plot) and Eq. (49) (right plot) for N_f=2 at β=2.10 as a function of $(a\,p)^2$ for each value of the pion mass before the pole subtraction. Lower panels: Eq. (48) (left plot) and Eq. (49) (right plot) for N_f=2 at β=2.10 as a function of $(a\,p)^2$ for each value of the pion mass after the pole subtraction.

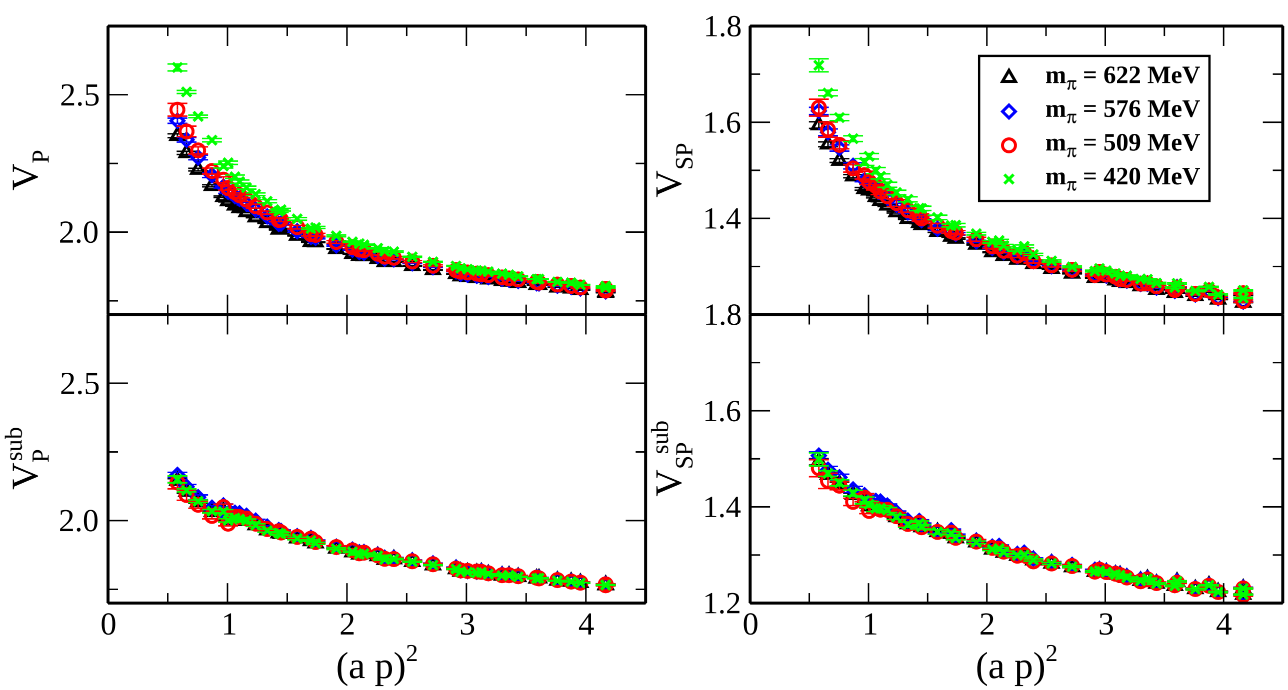

FIG. 14: As Fig. 13 but for the N_f=4 and β=2.10 ensembles.

C. $\overline{\text{MS}}$-scheme

In order to compare lattice values to experimental results one must convert to a universal renormalization scheme and use a reference renormalization scale. Typically one chooses the $\overline{\text{MS}}$-scheme at a scale μ of 2 GeV. For the conversion from the RI′ to the $\overline{\text{MS}}$ scheme we use the intermediate Renormalization Group Invariant (RGI) scheme, which is scale independent and relates the RI′ and $\overline{\text{MS}}$ results are follows:

$$Z_{\mathcal{O}}^{\rm RGI} = Z_{\mathcal{O}}^{\rm RI'}(\mu)\,\Delta Z_{\mathcal{O}}^{\rm RI'}(\mu) = Z_{\mathcal{O}}^{\overline{\rm MS}}(2\,{\rm GeV})\,\Delta Z_{\mathcal{O}}^{\overline{\rm MS}}(2\,{\rm GeV})\,. \tag{50}$$

The conversion factor can be read from the above relation:

$$Z_{\mathcal{O}}^{\overline{\rm MS}}(2\,{\rm GeV}) \equiv C_{\mathcal{O}}^{{\rm RI'},\overline{\rm MS}}(\mu, 2\,{\rm GeV})\,Z_{\mathcal{O}}^{\rm RI'}(\mu)\,, \qquad C_{\mathcal{O}}^{{\rm RI'},\overline{\rm MS}}(\mu, 2\,{\rm GeV}) = \frac{\Delta Z_{\mathcal{O}}^{\rm RI'}(\mu)}{\Delta Z_{\mathcal{O}}^{\overline{\rm MS}}(2\,{\rm GeV})}\,, \tag{51}$$

where the scheme dependent quantity $\Delta Z_{\mathcal{O}}^{\mathcal{S}}(\mu)$ can be expressed in terms of the β-function and the anomalous dimension, $\gamma_{\mathcal{O}}^{S} \equiv \gamma^{S}$ of the operator $\mathcal{O}$ (for definitions see Appendix A):

$$\Delta Z_{\mathcal{O}}^{\mathcal{S}}(\mu) = \left(2\beta_0 \frac{g^{\mathcal{S}}(\mu)^2}{16\pi^2}\right)^{-\frac{\gamma_0}{2\beta_0}} \exp\left\{\int_0^{g^{\mathcal{S}}(\mu)} {\rm d}g' \left(\frac{\gamma^{\mathcal{S}}(g')}{\beta^{\mathcal{S}}(g')} + \frac{\gamma_0}{\beta_0\, g'}\right)\right\}\,. \tag{52}$$

We employ the 3-loop approximation which simplifies to:

$$\begin{aligned}\Delta Z_{\mathcal{O}}^{\mathcal{S}}(\mu) = &\left(2\beta_0 \frac{g^{\mathcal{S}}(\mu)^2}{16\pi^2}\right)^{-\frac{\gamma_0}{2\beta_0}} \left(1 + \frac{g^{\mathcal{S}}(\mu)^2}{16\pi^2}\,\frac{\beta_1\gamma_0 - \beta_0\gamma_1^{S}}{2\beta_0^2} + \right. \\ &\left.\frac{g^{\mathcal{S}}(\mu)^4}{(16\pi^2)^2}\,\frac{-2\beta_0^3\gamma_2^S + \beta_0^2(\gamma_1^S(2\beta_1+\gamma_1^S) + 2\beta_2\gamma_0) - 2\beta_0\beta_1\gamma_0(\beta_1+\gamma_1^S) + \beta_1^2\gamma_0^2}{8\beta_0^4}\right),\end{aligned} \tag{53}$$

where the coupling constant, $g^{S}(\mu)$, is needed in both the $\overline{\text{MS}}$ and RI′ schemes; their expressions coincide to three loops and read [33] [3]:

$$\left.\frac{g^{\overline{\rm MS},{\rm RI'}}(\mu)^2}{16\pi^2}\right|_{3-{\rm loop}} = \frac{1}{\beta_0 L} - \frac{\beta_1}{\beta_0^3}\frac{\log L}{L^2} + \frac{1}{\beta_0^5}\frac{\beta_1^2\log^2 L - \beta_1^2 \log L + \beta_2\beta_0 - \beta_1^2}{L^3})\,, \quad L = \log\frac{\mu^2}{\Lambda_{\overline{\rm MS}}^2}\,. \tag{54}$$

For $\Lambda_{\overline{\rm MS}}$ we employ the value 315 MeV and 296 MeV for N_f=2 [34, 35] and N_f=4 [36], respectively.

VI. RESULTS

In this section, we present our results for the renormalization functions in the $\overline{\text{MS}}$ scheme at a scale of 2 GeV. The final data correspond to the non-perturbative values after subtracting the lattice artifacts to $\mathcal{O}(g^2\,a^\infty)$. Although, with the exception of $Z_{\rm P}$, the dependence of the RFs on the pion mass is not significant, we nevertheless perform a chiral extrapolation of the RFs using data at the same β and N_f ensembles obtained for different pion masses as discussed in subsection V A.

As can be seen in Figs. 16 - 23 the $\mathcal{O}(g^2\,a^\infty)$-subtracted RFs (magenta diamond points) have a very mild dependence on $(ap)^2$ which is almost linear, and it is removed by extrapolating to zero, using the Ansatz

$$Z_{\mathcal{O}}(a\,p) = Z_{\mathcal{O}}^{(0)} + Z_{\mathcal{O}}^{(1)}\cdot(a\,p)^2\,, \tag{55}$$

where $Z_{\mathcal{O}}^{(0)}$ corresponds to our final value on the renormalization functions. To extract the RFs reliably one needs to consider momenta in the range $\Lambda_{QCD} < p < 1/a$. We relax the upper bound to be $\sim 4/a$ to $7/a$, which is justified by the weak dependence of our results on $(a\,p)^2$. Therefore, for each value of β we consider momenta $(a\,p)^2 \geq 2$ for which perturbation theory is trustworthy and lattice artifacts are still small enough.

---

[3] Sign differences in some terms of Eq. (54) compared to Ref. [33] are related to alternative definition of the β-function

From our analysis we find that the data for the RFs depend not only on $(a\,p)^2$, but also on the directions of the momentum. Noting that, for democratic momenta (in all directions, not only spatial) the value of $p4/p2^2$ equals 0.25, we find empirically that data produced on momenta with the ratio of Eq. (44), $p4/p2^2$, being > 0.4, have a behavior that deviates from the general $(a\,p)^2$ curve. The choice of such a momentum ratio as a criterion is justified by the fact that such Lorentz non-invariant contributions appear in the perturbative computation at higher orders in the lattice spacing (e.g., $p4/p2$ for $\mathcal{O}(a^2)$). Thus, high values of this ratio are an indication of large lattice artifacts from higher loops. As an example, we demonstrate $Z_{\rm A}$ in Fig. 15 including the data obtained at momenta satisfying $P \equiv p4/p2 > 0.4$. These are shown by the filled blue circles and filled green diamonds corresponding to unsubtracted and $\mathcal{O}(g^2\,a^\infty)$-subtracted data, respectively. As can be seen, the filled symbols have different behavior than the open symbols. Although the subtraction of one-loop lattice artifacts reduces the difference, the higher order artifacts are not negligible. The data for these momenta have been excluded from the final analysis of all RFs. A similar study is presented in Refs. [14, 15].

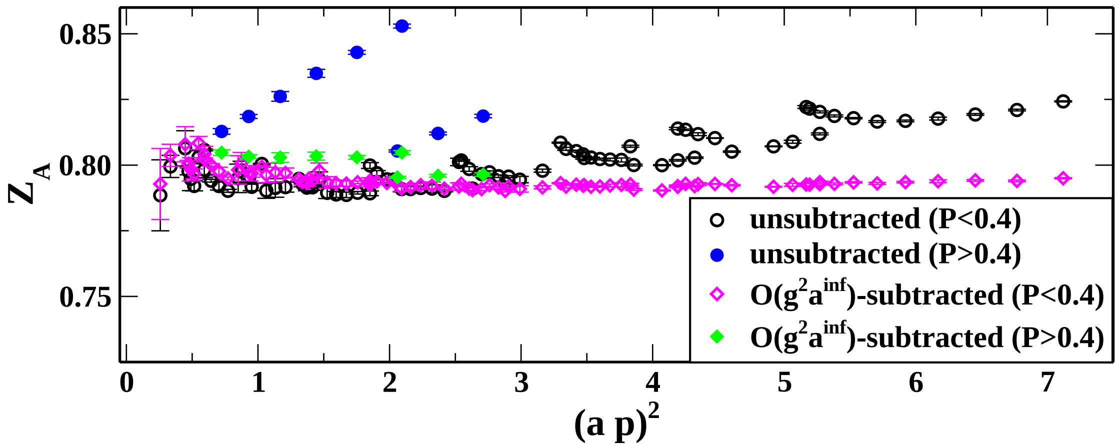

FIG. 15: $Z_{\rm A}$ as a function of the renormalization scale. Filled blue circles and filled green diamonds correspond to unsubtracted and $\mathcal{O}(g^2\,a^\infty)$-subtracted data using momenta with $P \equiv p4/p2 > 0.4$.

While statistical errors are very small, a careful investigation of systematic errors is required. A small systematic effect comes from the asymmetry of our lattices, both because they are larger in their time extent and because of the antiperiodic boundary conditions in the time direction. To address this issue, we average over the different components corresponding to the same RFs, for instance $Z_{\rm A}$ is defined as:

$$Z_{\rm A} \equiv \frac{1}{4}\left(Z_{\rm A}^0 + Z_{\rm A}^1 + Z_{\rm A}^3 + Z_{\rm A}^4\right) \tag{56}$$

where the upper index indicates the Dirac matrix used as current insertion ($Z_{\rm A}^i$ corresponds to insertion $\gamma_5\,\gamma_i$). In addition, remaining systematics are automatically removed by the subtraction of the $\mathcal{O}(g^2\,a^\infty)$ terms. The largest systematic error comes from the choice of the momentum range to use for the extrapolation to $a^2p^2 = 0$. One way to estimate this systematic error is to vary the lower or/and upper range used in the fit. Another approach is to fix a range and then eliminate a given momentum in the fit range and refit. The spread of the results about the mean gives an estimate of the systematic error. In the final results we give as systematic error the largest one from using these two procedures, which is the one obtained by modifying the fit range.

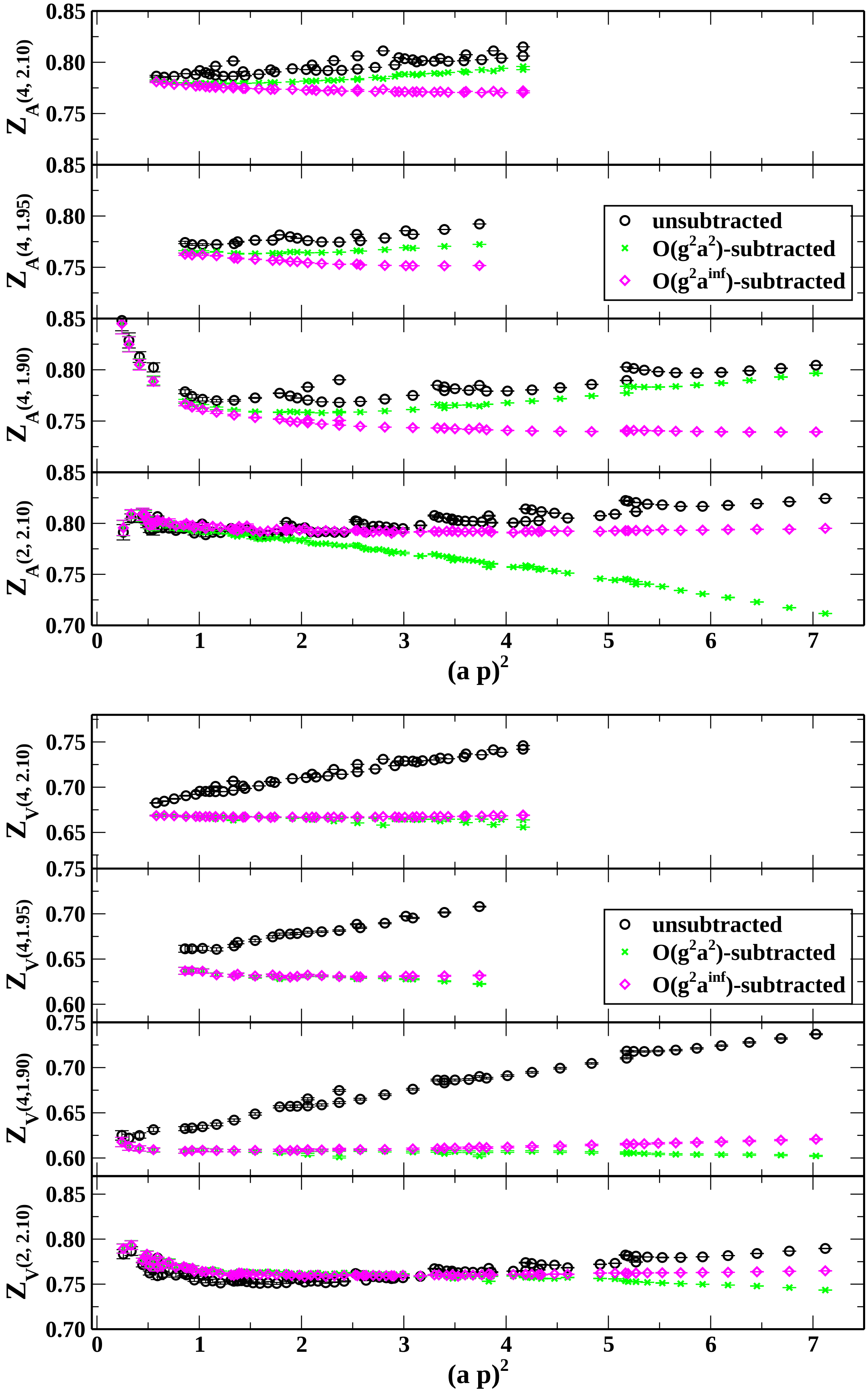

FIG. 16: $Z_{\rm A}$ (upper) and $Z_{\rm V}$ (lower) as a function of the renormalization scale. The arguments a, b of $Z(a, b)$ correspond to N_f and β, respectively. From top to bottom, the data correspond to increasing the lattice spacing. Non-perturbative values are shown with the black circles, $\mathcal{O}(g^2\,a^2)$-subtracted with the green crosses and $\mathcal{O}(g^2\,a^\infty)$-subtracted with magenta diamonds.

Fig. 16 corroborates that the magnitude of the lattice artifacts depends not only on the action parameters, but also on the operator under study, as can be seen for $Z_{\rm A}$ and $Z_{\rm V}$ shown for different values of the coupling constant. Since both $Z_{\rm V}$ and $Z_{\rm A}$ are scale independent, one expects a flat behavior as a function of the renormalization scale, $(a\,\mu)^2 = (a\,p)^2$. However, the non-perturbative data before subtraction of the lattice artifacts is carried out, exhibit a non-zero slope, which becomes negligible once the $\mathcal{O}(g^2\,a^\infty)$ terms are subtracted. For a proper comparison, we have kept the y-axis the same as the lattice spacing is increased. In the case of $Z_{\rm A}$ we find that the $\mathcal{O}(g^2\,a^2)$ terms computed for all N_f=4 gauge configurations, despite being the leading contributions, underestimate the total one-loop lattice artifacts, $\mathcal{O}(g^2\,a^\infty)$. Our analysis shows non-negligible lattice artifacts between $3-6\%$ for momenta in the range [2,4]. Nevertheless, for the N_f=2 case, the total one-loop lattice artifacts are very small $(0.1-2\%$ for $(a\,p)^2 : [2,4])$ which may be attributed to the inclusion of the clover term. One also observes that the $\mathcal{O}(g^2\,a^2)$ terms are no longer reliable, possibly due to the fact that they are polynomial functions of $c_{\rm sw}$ $(2-8\%$ for the aforementioned momentum range). This fact is an evidence that the addition of the clover term in the twisted mass action suppresses lattice artifacts. This is also observed for other quantities besides renormalization functions, such as in the isospin splitting in the Δ-system [37, 38].

For $Z_{\rm V}$, on the other hand, we find that for all ensembles analyzed in this work, there are negligible one-loop artifacts beyond $\mathcal{O}(g^2\,a^2)$, as can be seen in the lower panel of Fig. 16. From our study we find that lattice artifacs are current-dependent and can be identified *a posteriori*, from the perturbative computation. This is also confirmed by examining the results using the N_f=2 ensembles with the clover term shown in Figs. 17 - 23, where for $Z_{\rm P}$, the $\mathcal{O}(g^2\,a^2)$ and $\mathcal{O}(g^2\,a^\infty)$ are almost equivalent, especially for $(a\,p)^2 < 5$; This is not the case for the other RFs shown in Figs. 17 - 23. The N_f=2 are the most recent gauge configurations produced by ETMC, which are currently being used for hadron structure studies and thus the values of the RFs are needed to renormalize the hadron observables [39]. Figs. 17 -23 correspond to the RFs upon conversion to the $\overline{\rm MS}$ scheme at 2 GeV and are plotted against the initial renormalization scale, $(a\,p)^2$.

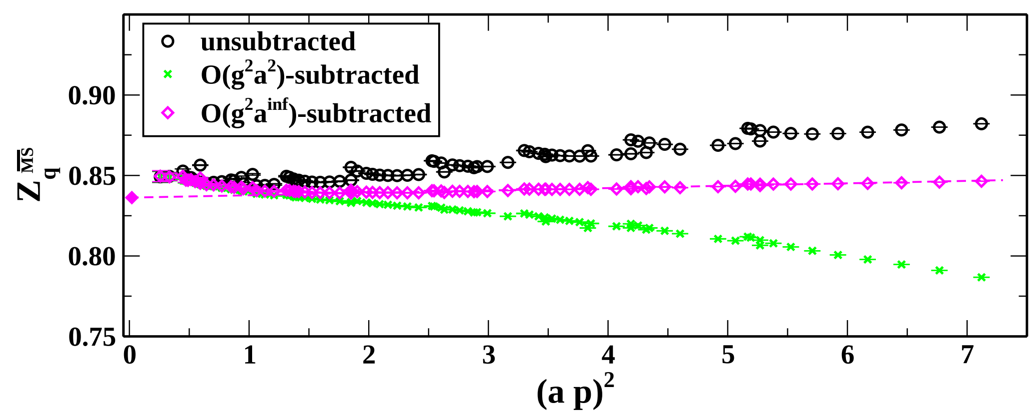

FIG. 17: Renormalization of the fermion field for N_f=2 twisted mass clover-improved fermions. The data correspond to the $\overline{\rm MS}$ scheme at a reference scale of 2 GeV and are plotted against the initial renormalization scale, $(a\,\mu)^2 = (a\,p)^2$. Black circles (magenta diamonds, green crossed) denote the unsubtracted ($\mathcal{O}(g^2\,a^\infty)$-subtracted, $\mathcal{O}(g^2\,a^2)$-subtracted) non-perturbative data.

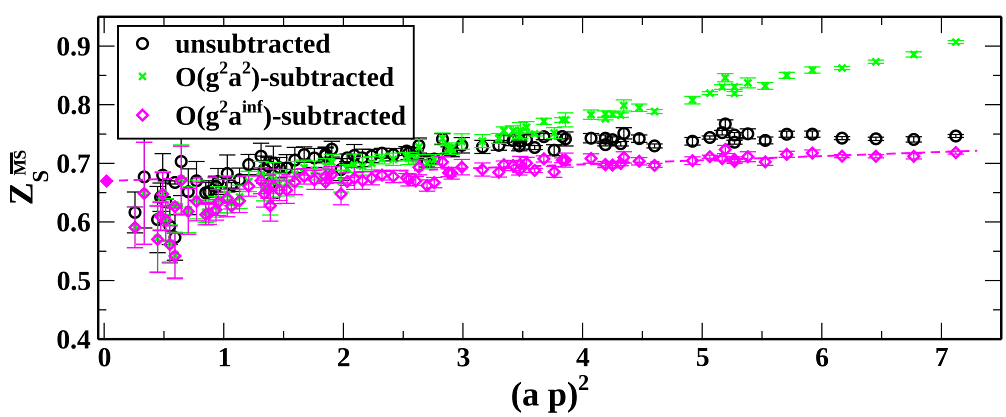

FIG. 18: The renormalization function of the scalar operator. The notation is the same as that of Fig. 17.

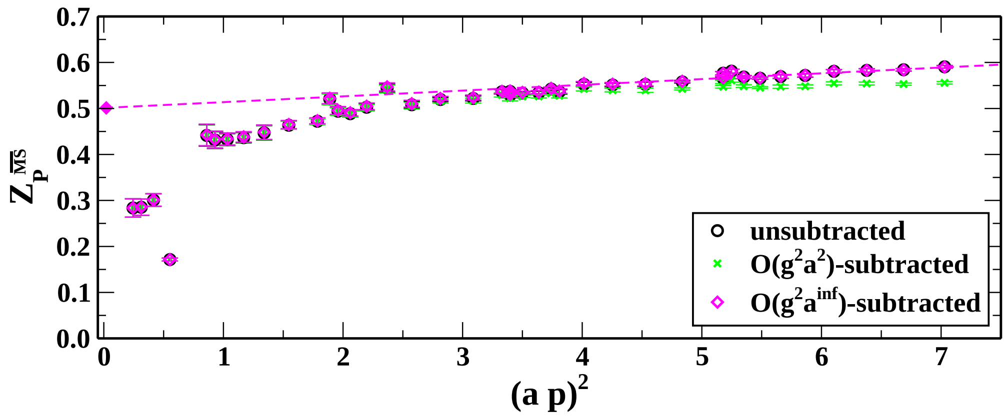

FIG. 19: Z_{P} after removal of the pion-pole term. The notation is the same as that of Fig. 17.

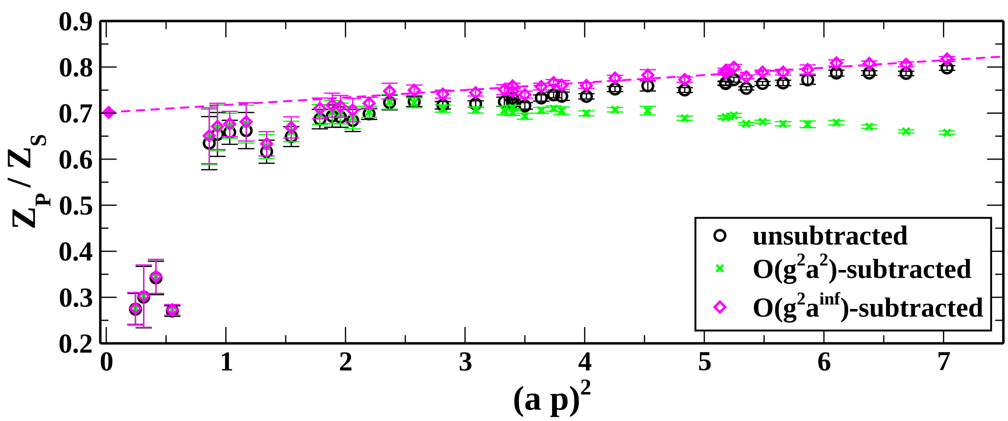

FIG. 20: The ratio $Z_{\mathrm{P}}/Z_{\mathrm{S}}$ after removal of the pion-pole term. The notation is the same as that of Fig. 17.

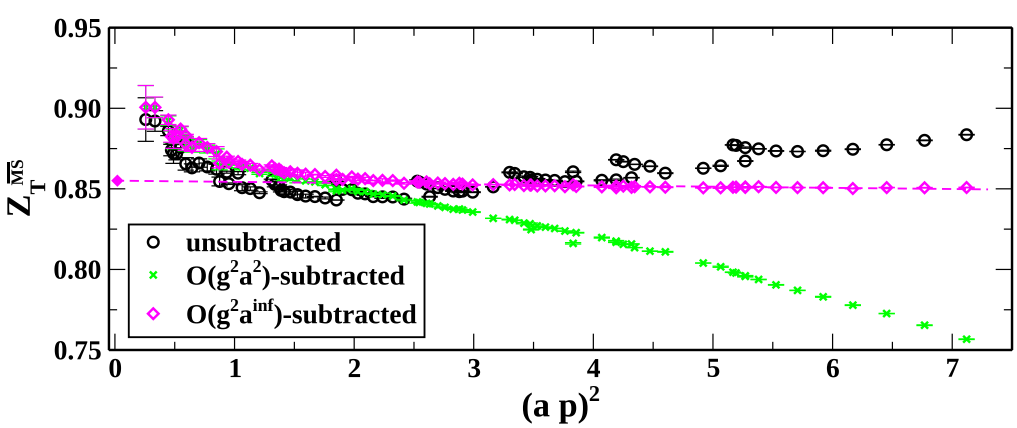

FIG. 21: The renormalization function of the tensor operator. The notation is the same as that of Fig. 17.

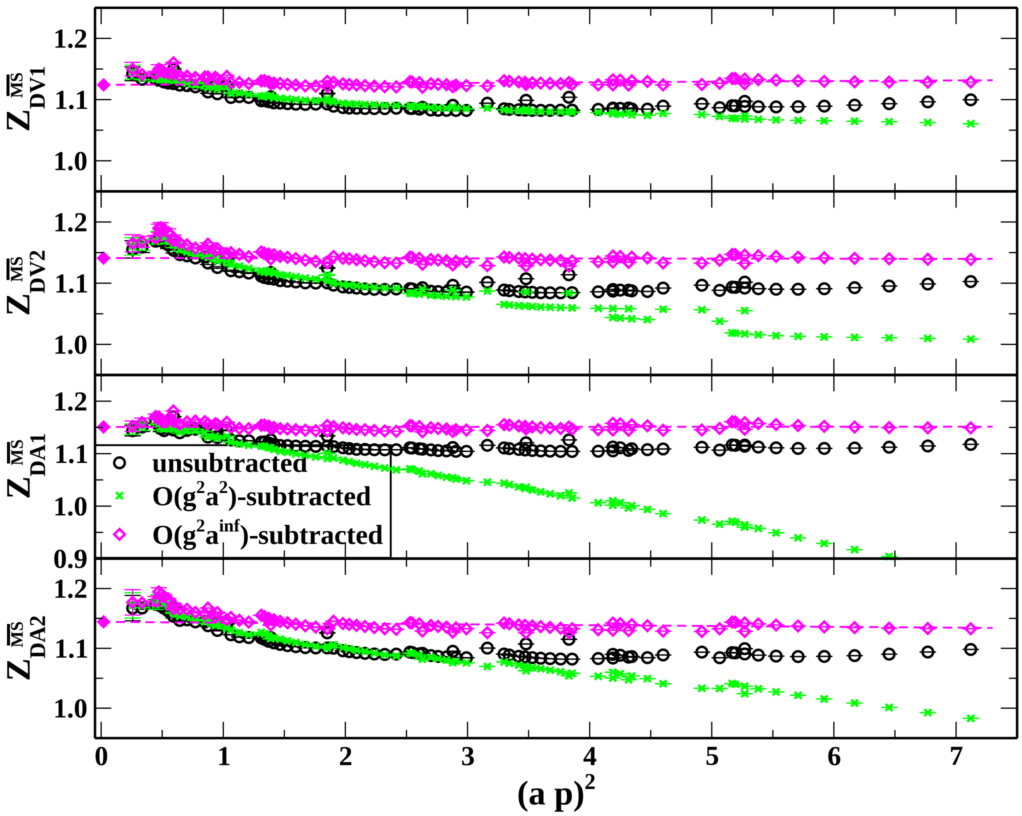

FIG. 22: The renormalization functions of the one-derivative vector and axial operators. The notation is the same as that of Fig. 17.

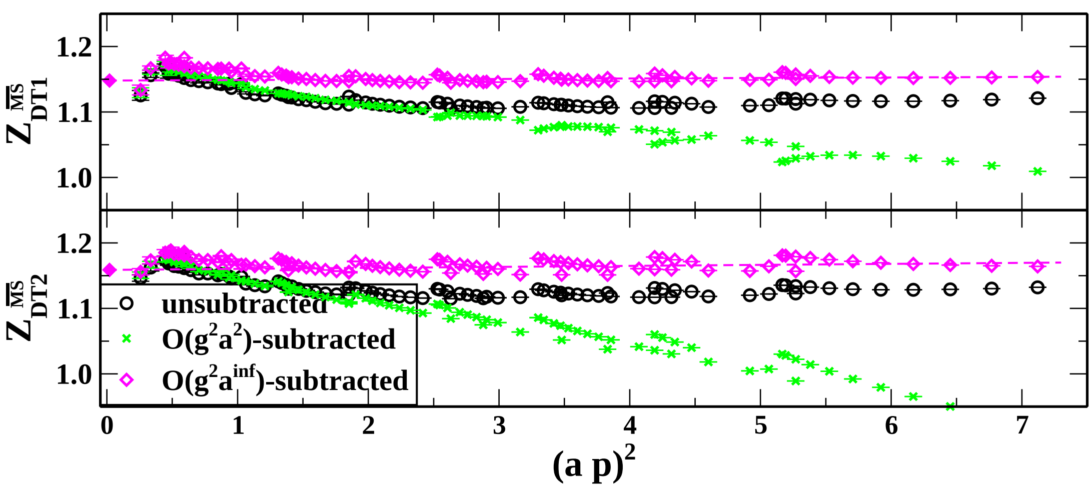

FIG. 23: The renormalization functions of the one-derivative tensor operators. The notation is the same as that of Fig. 17.

Comparing, for instance, $Z_{\rm V}$ and $Z_{\rm A}$ computed using the N_f=4 and N_f=2 ensembles (see Fig. 16), we find that the $\mathcal{O}(g^2\,a^\infty)$ lattice artifacts for the N_f=2 ensembles are smaller and lead to good quality plateaus. The extrapolation to $(a\,p)^2 \to 0$ is performed using the $\mathcal{O}(g^2\,a^\infty)$-subtracted data and for momenta with $(a\,p)^2 > 2$ which is the range of interest. The data display a very small slope thus leading to a good determination of the continuum value. For $Z_{\rm P}$ and $Z_{\rm P}/Z_{\rm S}$ there is a stronger dependence on $(a\,p)^2$ up to $(a\,p)^2 \sim 2-3$. Thus, for $Z_{\rm P}$ and $Z_{\rm P}/Z_{\rm S}$ we use a different interval for the $(a\,p)^2 \to 0$ fit. For instance, in the N_f=2 ensembles plotted here, we fit in the range [4,7] for $Z_{\rm P}$ and $Z_{\rm P}/Z_{\rm S}$, and in the range [2,7] for the remaining RFs. The systematic errors due to the choice of the fit, are computed by taking the difference in the values of $Z^{(0)}_{\mathcal{O}}$ (see Eq. (55)) extracted from these ranges and the range [3,5].

In Table III we give our final chiral extrapolated values of $Z^{(0)}_{\mathcal{O}}$ from $\mathcal{O}(g^2\,a^\infty)$-subtracted data (e.g. for N_f=2 the filled diamond point in Figs. 16 - 23). $Z_{\rm P}$ and $Z_{\rm P}/Z_{\rm S}$ are obtained only at β=2.10 (for both N_f=2, 4) where we have enough ensembles for the pion-pole subtraction; the corresponding results are presented in Table IV. Some of these RFs have been computed in Ref. [22]; the small differences observed between our results and those of Ref. [22] can be attributed to two factors: a) the different method for calculating non-perturbatively the vertex functions (see footnote 1) and b) the different analysis procedure since the authors use the subtraction of $\mathcal{O}(g^2_{boosted}\,a^2)$ lattice artifacts, which are, in general, larger than the $\mathcal{O}(g^2\,a^\infty)$ terms, leading, in some cases, to lower estimates. We have checked that if we apply the $\mathcal{O}(g^2_{boosted}\,a^2)$-subtraction to our non-perturbative estimates, we are in agreement with the results of Ref. [22]. Since the difference between our approach and that of Ref. [22] is the treatment of lattice artifacts, both sets of results should agree in the continuum limit, $a \to 0$. This is indeed the case, as demonstrated in Fig. 24 for the vector and axial RFs. Our results are also compared to those of Ref. [40]. We find that upon taking the continuum limit, the differences between the two works become very small, or compatible with zero. We note that in Ref. [40] the subtraction of lattice artifacts is performed via a hypercubic removal procedure. In addition, they use general momenta that are not restricted to democratic or near democtratic. Our results may also be compared with the data of Ref. [41], which are extracted from a three-loop calculation using numerical stochastic Perturbation Theory (NSPT). Of particular interest are their estimates for $Z_{\rm S}$, $Z_{\rm P}$, $Z_{\rm V}$, $Z_{\rm A}$ using Iwasaki gluons at β=1.95, 2.10. Although the authors employ N_f=4 Wilson fermions, at the chiral limit their results can be compared to ours. Such a comparison is quite interesting since both lattice artifacts and finite volume effects have been accounted in their fits. We find that, within error bars (statistical or systematic) the results of Ref. [41] are in agreement with our $\mathcal{O}(g^2\,a^\infty)$-subtracted data, for both values of β; this is an indication of a successful removal of the bulk of lattice artifacts. Regarding finite volume effects, a previous study using the twisted mass formulation shows very weak dependence [15].

RFs	N_f=2, β=2.10	N_f=4, β=2.10	N_f=4, β=1.95	N_f=4, β=1.90
$Z_{\rm q}^{\overline{\rm MS}}$	0.8366(2)(7)	0.7822(4)(4)	0.7835(2)(25)	0.7480(6)(11)
$Z_{\rm S}^{\overline{\rm MS}}$	0.6606(9)(18)	0.7143(9)(216)	0.7342(1)(21)	0.7835(2)(17)
$Z_{\rm V}$	0.7565(4)(19)	0.6651(2)(5)	0.6298(5)(29)	0.6015(2)(4)
$Z_{\rm A}$	0.7910(4)(5)	0.7744(7)(31)	0.7556(5)(85)	0.7474(6)(4)
$Z_{\rm T}^{\overline{\rm MS}}$	0.8551(2)(15)	0.7875(9)(15)	0.7483(6)(94)	0.7154(6)(6)
$Z_{\rm DV1}^{\overline{\rm MS}}$	1.1251(27)(17)	1.0991(29)(55)	1.0624(108)(33)	1.0268(26)(103)
$Z_{\rm DV2}^{\overline{\rm MS}}$	1.1396(16)(13)	1.1398(37)(91)	1.1209(61)(32)	1.0676(44)(190)
$Z_{\rm DA1}^{\overline{\rm MS}}$	1.1494(9)(99)	1.1741(42)(173)	1.1255(27)(328)	1.1151(51)(197)
$Z_{\rm DA2}^{\overline{\rm MS}}$	1.1357(20)(205)	1.1819(47)(147)	1.1555(36)(289)	1.1170(54)(223)
$Z_{\rm DT1}^{\overline{\rm MS}}$	1.1377(160)(13)	1.1562(32)(7)	1.1218(106)(44)	1.0777(37)(122)
$Z_{\rm DT2}^{\overline{\rm MS}}$	1.1472(121)(48)	1.1822(59)(118)	1.1727(121)(73)	1.0965(90)(278)

TABLE III: Our final values of the renormalization functions. The scheme and scale dependent RFs are given in $\overline{\rm MS}$ at 2 GeV. The number in the first parenthesis is the statistical error, while the number in the second parenthesis corresponds to the systematic error obtained by varying the fit range in the $(a\,p)^2 \to 0$ extrapolation.

RFs	N_f=2, β=2.10	N_f=4, β=2.10
$Z_{\rm P}^{\overline{\rm MS}}$	0.5012(75)(258)	0.5468(15)(176)
$Z_{\rm P}/Z_{\rm S}$	0.7016(141)(113)	0.7036(23)(195)

TABLE IV: Our final values for $Z_{\rm P}^{\overline{\rm MS}}(2\,{\rm GeV})$ and $Z_{\rm P}/Z_{\rm S}$. The number in the first parenthesis is the statistical error, while the number in the second parenthesis corresponds to the systematic error obtained by varying the fit range in the $(a\,p)^2 \to 0$ extrapolation.

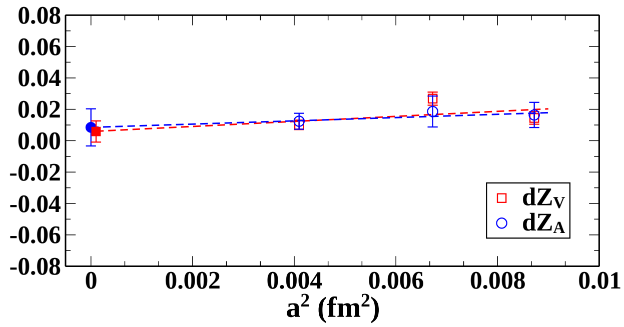

FIG. 24: Difference of $Z_{\rm V}$ and $Z_{\rm A}$ computed in this work and in Ref. [22] (Method 1) for the N_f=4 case. The data are plotted against the lattice spacing, and their extrapolation to the continuum limit is shown with a dashed line. Solid points correspond to the limit $a \to 0$; they are consistent with zero.

VII. CONCLUSIONS

We present results on the renormalization functions of the fermion field and fermion bilinears with up to one covariant derivative. The computation is performed non-perturbatively on several ensembles of N_f=4 twisted mass fermions, as well as N_f=2 twisted mass fermions including a clover term. This work is a continuation of our renormalization program first addressed in Refs. [14, 15]. Besides the analysis of the N_f=2 twisted mass clover-improved ensembles we have improved the procedure for the subtraction of lattice artifacts. The procedure that we adopt here for the perturbative computation of lattice artifacts is improved by taking into account not only leading order lattice artifacts, $\mathcal{O}(g^2\,a^2)$, but also contributions to all orders in the lattice spacing, $\mathcal{O}(g^2\,a^\infty)$.

The non-perturbative computation uses a momentum-dependent source and the RFs are extracted for all the relevant operators simultaneously. This leads to a very accurate evaluation of the RFs using only a small ensemble of gauge configurations ($\mathcal{O}(10)$). The precision of the results allows us to reliably investigate the quark mass dependence, which is found to be very weak with the exception of $Z_{\rm P}$. Nevertheless, a linear extrapolation with respect to the pion mass squared is carried out in order to reach the chiral limit. For the renormalization function of the pseudoscalar operator, $Z_{\rm P}$, we find a quark mass dependence due to the pion pole, which we eliminate using a refined procedure that avoids introduction of artificially large errors. The procedure entails a suitable fit (Eq. (45)) to identify $Z_{\rm P}$ directly from the constant term, a_P, instead of subtracting the pion-pole term (see Eq. (47)).

Our accurate non-perturbative results show that, although the lattice spacings considered in this work are smaller than 0.1 fm, lattice artifacts are not negligible in most cases, and are significantly larger than statistical errors. Thus, the subtraction of the $\mathcal{O}(g^2\,a^\infty)$ perturbative contributions appear to improve significantly the determination of the RFs, by leading to a milder dependence of the RFs on $(ap)^2$. Residual $\mathcal{O}(a^2p^2)$ effects are removed by extrapolating our results to $(ap)^2 = 0$. For the scheme and scale dependent RFs, we convert our values to the $\overline{\rm MS}$ scheme at a scale of 2 GeV. The statistical errors are, in general, smaller than the systematic ones. The latter are estimated by changing the window of values of the momentum used to extrapolate to $a^2p^2 = 0$. Our final values are given in Tables III - IV.

VIII. ACKNOWLEDGMENTS

We would like to thank all members of ETMC for a very constructive and enjoyable collaboration and for the fruitful discussions. This work used computational resources provided by PRACE, JSC, Germany as well as by the Cy-Tera machine at the Cyprus Institute. This work is in part supported by funding received from the Cyprus Research Promotion Foundation under contract ΝΕΑ ΥΠΟΔΟΜΗ/ΣΤΡΑΤΗ/0308/31 co-financed by the European Regional Development Fund. M.C. acknowledges financial support received from the Cyprus Research Promotion Foundation under contract TECHNOLOGY/ΘΕΠΙΣ/0311(ΒΕ)/16.

Appendix A: $\beta-$function and anomalous dimensions

For completeness we provide in this Appendix the definition of the $\beta-$function and the anomalous dimension of the operators studied in this work, which include up to one covariant derivative. To simplify the expressions we give the perturbative coefficients in the Landau gauge and in $SU(3)$.

The perturbative expansion of the anomalous dimension in a renormalization scheme $\mathcal{S}$ is given as follows:

$$\gamma^{\mathcal{S}} = -\mu \frac{\mathrm{d}}{\mathrm{d}\mu} \log Z_{\mathcal{S}} = \gamma_0 \frac{g^{\mathcal{S}}(\mu)^2}{16\pi^2} + \gamma_1^{\mathcal{S}} \left(\frac{g^{\mathcal{S}}(\mu)^2}{16\pi^2} \right)^2 + \gamma_2^{\mathcal{S}} \left(\frac{g^{\mathcal{S}}(\mu)^2}{16\pi^2} \right)^3 + \cdots \tag{A1}$$

Similarily, the $\beta-$function is defined as:

$$\beta^{\mathcal{S}} = \mu \frac{\mathrm{d}}{\mathrm{d}\mu} g^{\mathcal{S}}(\mu) = -\beta_0 \frac{g^{\mathcal{S}}(\mu)^3}{16\pi^2} - \beta_1 \frac{g^{\mathcal{S}}(\mu)^5}{(16\pi^2)^2} - \beta_2^{\mathcal{S}} \frac{g^{\mathcal{S}}(\mu)^7}{(16\pi^2)^3} + \cdots . \tag{A2}$$

For the conversion from the RI$'$ to the $\overline{\mathrm{MS}}$ scheme we use the three-loop expressions, to which the coefficients of the $\beta-$function coincide and are given by [42, 43]:

$$\beta_0 = 11 - \frac{2}{3} N_f \,, \tag{A3}$$
$$\beta_1 = 102 - \frac{38}{3} N_f \,, \tag{A4}$$
$$\beta_2 = \frac{2857}{2} - \frac{5033}{18} N_f + \frac{325}{54} N_f^2 \,. \tag{A5}$$

Below we give all necessary expressions to convert to the $\overline{\mathrm{MS}}$ scheme, as well as the references from which they were taken (see also references therein). Dome signs and multiplicative numerical factors have been adjusted to match the definition of Eq. (A1). An upper index appears for scheme-dependent quantities, in order to denote the scheme that they correspond to.

Quark field [44]:

$$\gamma_0 = 0 \,, \tag{A6}$$
$$\gamma_1 = \frac{134}{3} - \frac{8}{3} N_f \,, \tag{A7}$$
$$\gamma_2^{\overline{\mathrm{MS}}} = \frac{20729}{18} - 79\zeta_3 - \frac{1100}{9} N_f + \frac{40}{27} N_f^2 \,, \tag{A8}$$
$$\gamma_2^{\mathrm{RI}'} = \frac{52321}{18} - 79\zeta_3 - \frac{1100}{9} N_f + \frac{40}{27} N_f^2 \,, \tag{A9}$$

($\zeta_3 = 1.20206...$)

Scalar/pseudoscalar [45, 46]:

$$\gamma_0 = -8 \,, \tag{A10}$$
$$\gamma_1^{\overline{\mathrm{MS}}} = -\frac{404}{3} + \frac{40}{9} N_f \,, \tag{A11}$$
$$\gamma_1^{\mathrm{RI}'} = -252 + \frac{104}{9} N_f \,, \tag{A12}$$
$$\gamma_2^{\overline{\mathrm{MS}}} = -2498 + \left(\frac{4432}{27} + \frac{320}{3}\zeta_3 \right) N_f + \frac{280}{81} N_f^2 \,, \tag{A13}$$
$$\gamma_2^{\mathrm{RI}'} = -\frac{40348}{3} + \frac{6688}{3}\zeta_3 + \left(\frac{35176}{27} - \frac{256}{9}\zeta_3 \right) N_f - \frac{1712}{81} N_f^2 \,, \tag{A14}$$

Tensor [43, 47]:

$$\gamma_0 = \frac{8}{3} \,, \tag{A15}$$
$$\gamma_1 = \frac{724}{9} - \frac{104}{27} N_f \,, \tag{A16}$$
$$\gamma_2^{\overline{\mathrm{MS}}} = \frac{105110}{81} - \frac{1856}{27}\zeta_3 - \left(\frac{10480}{81} + \frac{320}{9}\zeta_3 \right) N_f - \frac{8}{9} N_f^2 \,, \tag{A17}$$
$$\gamma_2^{\mathrm{RI}'} = \frac{359012}{81} - \frac{26144}{27}\zeta_3 + \left(-\frac{39640}{81} + \frac{512}{27}\zeta_3 \right) N_f + \frac{2288}{243} N_f^2 \,. \tag{A18}$$

One-derivative vector/axial [30, 48]:

$$\gamma_0 = \frac{64}{9}\,, \tag{A19}$$

$$\gamma_1^{\overline{\rm MS}} = \frac{23488}{243} - \frac{512}{81} N_f\,, \tag{A20}$$

$$\gamma_1^{\rm RI'} = \frac{48040}{243} - \frac{112}{9} N_f\,, \tag{A21}$$

$$\gamma_2^{\overline{\rm MS}} = \frac{11028416}{6561} + \frac{2560}{81}\zeta_3 - \left(\frac{334400}{2187} + \frac{2560}{27}\zeta_3\right) N_f - \frac{1792}{729} N_f^2\,, \tag{A22}$$

$$\gamma_2^{\rm RI'} = \frac{59056304}{6561} - \frac{103568}{81}\zeta_3 - \left(\frac{2491456}{2187} + \frac{416}{27}\zeta_3\right) N_f + \frac{19552}{729} N_f^2\,. \tag{A23}$$

One-derivative tensor [48]:

$$\gamma_0 = 8\,, \tag{A24}$$

$$\gamma_1^{\overline{\rm MS}} = 124 - 8\,N_f\,, \tag{A25}$$

$$\gamma_1^{\rm RI'} = \frac{680}{3} - \frac{128}{9} N_f\,, \tag{A26}$$

$$\gamma_2^{\overline{\rm MS}} = \frac{19162}{9} - \left(\frac{5608}{27} + \frac{320}{3}\zeta_3\right) N_f - \frac{184}{81} N_f^2\,, \tag{A27}$$

$$\gamma_2^{\rm RI'} = \frac{97052}{9} - \frac{4312}{3}\zeta_3 - \left(\frac{36848}{27} + \frac{176}{9}\zeta_3\right) N_f + \frac{2624}{81} N_f^2\,. \tag{A28}$$

Appendix B: Application of the subtraction to $\mathcal{O}(g^2\,a^\infty)$ in other ensembles

As discussed in the main part of the paper in our previous works of Refs. [14, 15] we have applied a procedure of subtracting the lattice artifacts of $\mathcal{O}(g^2\,a^2)$. The values of the RFs are used to renormalize hadron quantities such as the axial charge and the quark momentum fraction, in order to compare them with other lattice discretizations, as well as with experimental data. For a fair comparison between renormalized matrix elements of the ensembles presented in this work and the ones given in Refs. [14, 15], we have updated the RFs of the latter publications by applying the subtraction procedure to one-loop and all orders in the lattice spacing, $\mathcal{O}(g^2\,a^\infty)$. These correspond to tree-level Symanzik improved gauge action and N_f=2 twisted mass fermions at three values of the coupling constant corresponding to β=3.90, 4.05, 4.20. Since the gluon action is different from the ensembles of Table II, and since employed momentum values are also different, a perturbative computation of the $\mathcal{O}(g^2\,a^\infty)$ contributions was required on each ensemble in order to match its parameters, such as the coupling constant, the lattice size and the values of the renormalization scales. The new data on the Rfs are given in Table V.

RFs	$\beta = 3.9$	$\beta = 4.05$	$\beta = 4.20$
$Z_{\rm q}^{\overline{\rm MS}}$	0.769(1)(2)	0.787(1)(3)	0.783(1)(2)
$Z_{\rm S}^{\overline{\rm MS}}$	0.791(2)(41)	0.748(2)(31)	0.754(1)(16)
$Z_{\rm P}^{\overline{\rm MS}}$	0.527(6)(70)	0.517(2)(33)	0.546(5)(33)
$Z_{\rm P}/Z_{\rm S}$	0.672(7)(60)	0.700(3)(14)	0.731(5)(25)
$Z_{\rm V}$	0.646(2)(2)	0.681(2)(6)	0.701(1)(4)
$Z_{\rm A}$	0.769(2)(1)	0.787(1)(1)	0.791(1)(1)
$Z_{\rm T}^{\overline{\rm MS}}$	0.758(2)(4)	0.796(1)(3)	0.814(1)(3)
$Z_{\rm DV1}^{\overline{\rm MS}}$	1.028(2)(6)	1.080(2)(11)	1.087(3)(12)
$Z_{\rm DV2}^{\overline{\rm MS}}$	1.064(4)(4)	1.123(4)(10)	1.130(4)(4)
$Z_{\rm DA1}^{\overline{\rm MS}}$	1.106(3)(8)	1.157(4)(10)	1.150(4)(15)
$Z_{\rm DA2}^{\overline{\rm MS}}$	1.102(5)(7)	1.161(4)(13)	1.164(3)(6)

TABLE V: Updated results on the RFs of Refs. [14, 15] (N_f=2, β=3.90, 4.05, 4.20, $c_{\rm sw} = 0$) using the subtraction procedure to $\mathcal{O}(g^2\, a^\infty)$.

[1] M. Constantinou, PoS **LATTICE2014**, 001 (2014), [arXiv:1411.0078].
[2] C. Alexandrou, E. Gregory, T. Korzec, G. Koutsou, J. W. Negele, T. Sato, and A. Tsapalis, Phys. Rev. Lett. **107**, 141601 (2011), [arXiv:1106.6000].
[3] T. T. Takahashi and T. Kunihiro, Phys. Rev. **D78**, 011503 (2008), [arXiv:0801.4707].
[4] H.-W. Lin and K. Orginos, Phys. Rev. **D79**, 034507 (2009), [arXiv:0712.1214].
[5] G. Erkol, M. Oka, and T. T. Takahashi, Phys. Lett. **B686**, 36 (2010), [arXiv:0911.2447].
[6] C. Alexandrou, K. Hadjiyiannakou, K. Jansen, and C. Kallidonis (ETM Collaboration), PoS **Lattice2013**, 279 (2014), [arXiv:1404.6355].
[7] M. Constantinou, M. Costa, R. Frezzotti, V. Lubicz, G. Martinelli, D. Meloni, H. Panagopoulos, and S. Simula (ETM Collaboration), PoS **Lattice2014**, 390 (2014), [arXiv:1412.1351].
[8] M. Constantinou, M. Costa, R. Frezzotti, V. Lubicz, G. Martinelli, D. Meloni, H. Panagopoulos, and S. Simula (ETM Collaboration), Phys. Rev. **D92**, 034505 (2015), [arXiv:1506.00361].
[9] C. Alexandrou, V. Drach, K. Hadjiyiannakou, K. Jansen, B. Kostrzewa, and C. Wiese, PoS **LATTICE2013**, 289 (2014), [arXiv:1311.3174].
[10] C. Alexandrou et al. (ETM Collaboration), in preparation (2015).
[11] R. Frezzotti, P. A. Grassi, S. Sint, and P. Weisz (Alpha collaboration), JHEP **0108**, 058 (2001), [hep-lat/0101001].
[12] G. Martinelli, C. Pittori, C. T. Sachrajda, M. Testa, and A. Vladikas, Nucl. Phys. **B445**, 81 (1995), [hep-lat/9411010].
[13] C. Sturm, Y. Aoki, N. H. Christ, T. Izubuchi, C. T. C. Sachrajda, and A. Soni, Phys. Rev. **D80**, 014501 (2009), 0901.2599.
[14] C. Alexandrou, M. Constantinou, T. Korzec, H. Panagopoulos, and F. Stylianou (ETM Collaboration), Phys. Rev. **D83**, 014503 (2011), [arXiv:1006.1920].
[15] C. Alexandrou, M. Constantinou, T. Korzec, H. Panagopoulos, and F. Stylianou (ETM Collaboration), Phys. Rev. **D86**, 014505 (2012), [arXiv:1201.5025].
[16] B. Blossier et al. (ETM Collaboration), PoS **LATTICE2011**, 233 (2011), [arXiv:1112.1540].
[17] A. Abdel-Rehim et al. (ETM Collaboration), PoS **LATTICE2014**, 119 (2014), [arXiv:1411.6842].
[18] C. Alexandrou, M. Constantinou, S. Dinter, V. Drach, K. Jansen, C. Kallidonis, and G. Koutsou (ETM Collaboration), Phys. Rev. **D88**, 014509 (2013), [arXiv:1303.5979].
[19] A. Abdel-Rehim et al. (ETM Collaboration), PoS **LATTICE2013**, 264 (2014), [arXiv:1311.4522].
[20] P. Dimopoulos, R. Frezzotti, G. Herdoiza, K. Jansen, V. Lubicz, D. Palao, and G. Rossi (ETM Collaboration), PoS **LATTICE2010**, 235 (2010), [arXiv:1101.1877].
[21] R. Frezzotti and G. C. Rossi, JHEP **08**, 007 (2004), [hep-lat/0306014].
[22] N. Carrasco et al. (ETM Collaboration), Nucl. Phys. **B887**, 19 (2014), [arXiv:1403.4504].
[23] P. Weisz, Nucl. Phys. **B212**, 1 (1983).
[24] P. Dimopoulos and R. Frezzotti, private communication.
[25] A. Abdel-Rehim, C. Alexandrou, M. Constantinou, K. Hadjiyiannakou, K. Jansen, and G. Koutsou (ETM Collaboration), PoS **Lattice2014**, 148 (2015), [arXiv:1501.01480].
[26] R. Arthur and P. A. Boyle (RBC, UKQCD), Phys. Rev. **D83**, 114511 (2011), 1006.0422.
[27] M. Göckeler, R. Horsley, H. Oelrich, H. Perlt, D. Petters, P. Rakow, A. Schäfer, G. Schierholz, and A. Schiller (QCDSF Collaboration), Nucl. Phys. **B544**, 699 (1999), [hep-lat/9807044].

[28] P. de Forcrand, Nucl. Phys. Proc. Suppl. **9**, 516 (1989).
[29] M. Constantinou, V. Lubicz, H. Panagopoulos, and F. Stylianou, JHEP **0910**, 064 (2009), [arXiv:0907.0381].
[30] M. Göckeler et al. (QCDSF Collaboration), Phys. Rev. **D82**, 114511 (2010), [Erratum: Phys. Rev. D86, 099903 (2012)], [arXiv:1003.5756].
[31] M. Constantinou, M. Costa, M. Göckeler, R. Horsley, H. Panagopoulos, H. Perlt, P. Rakow, G. Schierholz, and A. Schiller (QCDSF Collaboration), Phys. Rev. **D87**, 096019 (2013), [arXiv:1303.6776].
[32] M. Constantinou, R. Horsley, H. Panagopoulos, H. Perlt, P. Rakow, G. Schierholz, A. Schiller, and J. Zanotti (QCDSF Collaboration), Phys. Rev. **D91**, 014502 (2015), [arXiv:1408.6047].
[33] A. I. Alekseev, Few Body Syst. **32**, 193 (2003), [hep-ph/0211339].
[34] K. Jansen, F. Karbstein, A. Nagy, and M. Wagner (ETM Collaboration), JHEP **1201**, 025 (2012), [arXiv:1110.6859].
[35] P. Fritzsch, F. Knechtli, B. Leder, M. Marinkovic, S. Schäfer, R. Sommer, and V. Virotta, Nucl. Phys. **B865**, 397 (2012), [arXiv:1205.5380].
[36] K. A. Olive et al. (Particle Data Group), Chin. Phys. **D38**, 090001 (2014).
[37] C. Alexandrou, M. Constantinou, K. Hadjiyiannakou, K. Jansen, C. Kallidonis, and G. Koutsou (ETM Collaboration), PoS **LATTICE2014**, 151 (2015), [arXiv:1411.3494].
[38] C. Alexandrou, V. Drach, K. Hadjiyiannakou, K. Jansen, C. Kallidonis, and G. Koutsou (ETM Collaboration), PoS **LATTICE2014**, 100 (2015), [arXiv:1412.0925].
[39] A. Abdel-Rehim et al. (ETM Collaboration) (2015), arXiv:1507.04936.
[40] B. Blossier, M. Brinet, P. Guichon, V. Morenas, O. Pene, J. Rodrguez-Quintero, and S. Zafeiropoulos (ETM Collaboration), Phys. Rev. **D91**, 114507 (2015), [arXiv:1411.1109].
[41] M. Brambilla, F. Di Renzo, and M. Hasegawa, Eur. Phys. J. **C74**, 2944 (2014), [arXiv:1402.6581].
[42] T. van Ritbergen, J. Vermaseren, and S. Larin, Phys. Lett. **B400**, 379 (1997), [hep-ph/9701390].
[43] J. Gracey, Nucl. Phys. **B662**, 247 (2003), [hep-ph/0304113].
[44] K. Chetyrkin and A. Retey, Nucl. Phys. **B583**, 3 (2000), [hep-ph/9910332].
[45] K. Chetyrkin, Phys. Lett. **B404**, 161 (1997), [hep-ph/9703278].
[46] J. Vermaseren, S. Larin, and T. van Ritbergen, Phys. Lett. **B405**, 327 (1997), [hep-ph/9703284].
[47] J. Gracey, Phys. Lett. **B488**, 175 (2000), [hep-ph/0007171].
[48] J. Gracey, Nucl. Phys. **B667**, 242 (2003), [hep-ph/0306163].